submitted to *Geophys. J. Int.*

A reappraisal of active tectonics along the Fethiye-Burdur trend, southwestern Turkey

Edwin Nissen[1], Musavver Didem Cambaz[2], Élyse Gaudreau[1], Andrew Howell[3,4], Ezgi Karasözen[5,6], and Elena Savidge[1,6]

[1] *School of Earth and Ocean Sciences, University of Victoria, Victoria BC, Canada*

[2] *Regional Earthquake Tsunami Monitoring Center, Kandilli Observatory and Earthquake Research Institute, Boğaziçi University, 34684 Çengelköy, İstanbul, Turkey*

[3] *School of Earth and Environment, University of Canterbury, Christchurch 8140, New Zealand*

[4] *GNS Science, Lower Hutt 5040, New Zealand*

[5] *Alaska Earthquake Center, University of Alaska Fairbanks, Fairbanks, Alaska 99775, USA*

[6] *Department of Geophysics, Colorado School of Mines, Golden, Colorado 80401, USA*

Received 2022 January 12; in original form 2021 July 6

SUMMARY

We investigate active tectonics in southwestern Turkey along the trend between Fethiye, near the eastern end of the Hellenic subduction zone, and Burdur, on the Anatolian plateau. Previously, regional GNSS velocities have been used to propose either (1) a NE-trending zone of strike-slip faulting coined the Fethiye-Burdur Fault Zone, or (2) a mix of uniaxial and radial extension accommodated by normal faults with diverse orientations. We test these models against the available earthquake data, updated in light of recent earthquakes at Arıcılar (24 November 2017, M_w 5.3), Acıpayam (20 March 2019, M_w 5.6) and Bozkurt (8 August 2019, M_w 5.9), the largest in this region in the last two decades. Using Sentinel-1 InSAR and seismic waveforms and arrival times, we show that the Arıcılar, Acıpayam, and Bozkurt earthquakes were partially or fully buried ruptures on pure normal faults with subtle or indistinct topographic expressions. By exploiting ray paths shared with these well-recorded modern events, we relocate earlier instrumental seismicity throughout southwestern Turkey and incorporate these improved hypocenters in an updated focal mechanism compilation. The southwestern Fethiye-Burdur trend is dominated by ESE-WNW trending normal faulting, even though most faults evident in the topography strike NE-SW. This hints at a recent change in regional strain, perhaps related to eastward propagation of the Gökova graben into the area or to rapid subsidence of the Rhodes basin. The northeastern Fethiye-Burdur trend is characterized by orthogonal normal faulting, consistent with radial extension and likely responsible for the distinct physiography of Turkey's Lake District. We find that the 1971 M_w 6.0 Burdur earthquake likely ruptured a NW-dipping normal fault in an area of indistinct geomorphology near Salda Lake, contradicting earlier studies that place it on well-expressed faults bounding the Burdur basin, and further highlighting how damaging earthquakes are possible on faults that would prove difficult to identify beforehand. Overall, our results support GNSS-derived kinematic models that depict a mix of uniaxial and radial extension throughout southwestern Turkey, with no evidence from focal mechanisms for major, active strike-slip faults anywhere along the Fethiye-Burdur trend. Normal faulting orientations are consistent with a stress field driven primarily by contrasts in gravitational potential energy between the elevated Anatolian plateau and the low-lying Rhodes and Antalya basins.

Key words: Seismicity and tectonics, earthquake source observations, satellite geodesy, continental neotectonics, earthquake hazards

1 INTRODUCTION

Southwestern Turkey is characterized by active crustal faulting and abundant seismicity, but the kinematics and dynamics of this deformation are both controversial. The region sits atop two arcuate, northward-dipping subduction zones — the Hellenic and Cyprus arcs — in which Nubian oceanic lithosphere is consumed beneath continental Anatolia (Figure 1a). The easternmost Hellenic subduction zone is characterized by parallel, NE-trending bathymetric troughs termed the Pliny and Strabo trenches, which are highly oblique to Nubia–Anatolia plate convergence and may involve some component of sinistral strike-slip faulting (McKenzie 1972; Hall et al. 2009; Shaw & Jackson 2010; Özbakır et al. 2013). It has been proposed that these faults continue across the Rhodes Basin and into Anatolia (Ocakoğlu 2012; Hall et al. 2014) to form a NE-trending zone of discontinuous, sinistral or sinistral-transtensional faults termed the Fethiye-Burdur Fault Zone (FBFZ) (e.g. Dumont et al. 1979; Eyidogan & Barka 1996; Barka & Reilinger 1997; Tiryakioğlu et al. 2013; Elitez et al. 2015, 2016) after the cities of Fethiye, on the Mediterranean coastline, and Burdur, on the Anatolian plateau (yellow squares, Figure 1a–b). These purported sinistral faults constitute the western limb of a triangular structural trend known as the Isparta angle.

However, existence of the sinistral FBFZ has been called into question, with a number of geological, seismological and geodetic studies pointing to a dominance of crustal extension and normal faulting along the Fethiye-Burdur trend (e.g. Koçyiğit & Özacar 2003; Över et al. 2010, 2013b; Alçiçek 2015; Howell et al. 2017; Kaymakcı et al. 2018; Özkaptan et al. 2018) and indeed throughout the Isparta angle (Glover & Robertson 1998; Över et al. 2016). Resolving this discrepancy is important for understanding regional earthquake risks, with several faults of disputed slip sense and rate included in Turkey's most recent national active fault database (Emre et al. 2018) and probabilistic seismic hazard maps (Demircioğlu et al. 2018). Linkage between onshore faults and offshore faulting in the Rhodes basin may also have important implications for regional tsunami hazards (England et al. 2015; Howell et al. 2015). Finally, accurately characterizing fault kinematics is crucial to understanding what is driving the deformation, whether it be plate boundary forces (Jiménez-Munt & Sabadini 2002; Reilinger et al. 2006), contrasts in gravitational potential energy between thickened continental crust of the Anatolian plateau and low-lying oceanic lithosphere of the Mediterranean basin (England et al. 2016), or a mixture of the two (Özeren & Holt 2010).

Earthquakes provide a powerful means of assessing the regional kinematics and the prevalence of strike-slip faulting. The 24 November 2017 M_w 5.3 Arıcılar earthquake, the 20 March 2019 M_w 5.6 Acıpayam earthquake, and the 8 August 2019 M_w 5.9 Bozkurt earthquake (Figure 1b) were the largest within the Isparta angle in more than two decades and were each captured by satellite-borne Interferometric Synthetic Aperture Radar (InSAR) as well as by regional and teleseismic waveforms and arrival times. The goal of this paper is to exploit these well-recorded modern earthquake sequences in a reassessment of regional active tectonics. We examine the whole Isparta angle, though our principal focus is the Fethiye-Burdur trend along its western limb.

In Section 2, we briefly review previous evidence for and against the existence of a left-lateral FBFZ. In Section 3, we describe the geodetic and seismological data and modelling approaches used to characterize the modern earthquakes, and discuss a catalogue of regional focal mechanisms compiled from the literature and updated with new, relocated hypocenters. Finding a distinct change in the pattern of earthquake faulting approximately midway between Fethiye and Burdur, we separate our results geographically. In Section 4, we examine seismicity in the southern Isparta angle with a focus on the Fethiye region; this includes the first ever detailed analysis of the 2017 Arıcılar sequence. In Section 5, we investigate seismicity in the northern Isparta angle; this includes new assessments of the 2019 Acıpayam and Bozkurt sequences and a reexamination of the destructive 12 May 1971 M_w 6.0 Burdur earthquake. In Section 6, we first discuss the new earthquake data in light of GNSS-derived regional kinematic models and then consider the forces likely responsible for the observed deformation.

2 A SUMMARY OF EVIDENCE FOR AND AGAINST THE FBFZ

2.1 Surface geology and subsurface geophysics

Dumont et al. (1979) first proposed that prominent NE-trending faults in southwestern Turkey constituted a major, sinistral strike-slip zone associated with the eastern termination of the Hellenic arc. However, despite an abundance of subsequent mapping and surveying, the geological and geophysical evidence for the FBFZ remains inconclusive.

Ocakoğlu (2012) and Hall et al. (2014) studied the Rhodes Basin and Gulf of Fethiye (Figure 1b) using multi-beam bathymetry and seismic reflection imagery, identifying several NE-trending faults and linking them kinematically with the purported FBFZ onshore. However, Tosun et al. (2021) later characterized faults in and around the Gulf of Fethiye as predominantly normal sense. East and north of Fethiye, ten Veen (2004), Elitez & Yaltırak (2014, 2016) and Elitez et al. (2017) mapped distributed, NE-trending, sinistral-transtensional faults in the Eşen-Çay, Çameli and Gölhisar basins (Figure 1b). However, Alçiçek et al. (2006) and Özkaptan et al. (2018) have argued for normal motions on faults near Çameli and the purported sinistral components remain controversial (Alçiçek 2015; Elitez et al. 2015). A paleoseismic study of the Acıpayam fault, one of the longest NE-trending strutures in this area (Figure 1b), also suggested predominantly normal kinematics (Kürçer et al. 2016). Gürer et al. (2004) conducted a magnetotelluric profile across this region and attributed a zone of high conductivity southeast of Çameli to the FBFZ, but these data lack kinematic indicators. Paleomagnetic data from Kaymakcı et al. (2018) do not support a major strike-slip fault in this region.

Further northeast, Aksoy & Aksarı (2016) characterized NE-trending faults bounding the Tefenni basin as sinistral-transtensional while Price & Scott (1994) described those in the nearby Burdur, Acıgöl and Baklan basins as being normal with sinistral components (Figure 1b). However, a large fault slickenside dataset compiled by Özkaptan et al. (2018) suggested that the largest faults in the Burdur region are predominantly normal sense, with transtensional slip limited to smaller NW-trending faults in transfer zones between the major NE-trending extensional basins. A M_S 7.0 earthquake on 3 October 1914, which caused widespread devastation across Burdur basin and killed $\sim$4,000 people, involved NE-trending normal or normal-dextral faults along the SE shoreline of Lake Burdur, where it likely ruptured to the surface (Taymaz & Price 1992; Ambraseys & Jackson 1998). Northeast of the Burdur region, many of the most prominent active structures trend NW-SE (perpendicular to the FBFZ) and involve normal kinematics. These include the Dinar fault and the Akşehir-Afyon graben, which ruptured to the surface in the 1995 M_w 6.5 Dinar and 2002 M_w 6.4 Çay earthquakes, respectively (Eyidogan & Barka 1996; Koçyiğit & Özacar 2003).

2.2 Earthquake focal mechanisms

Earthquake focal mechanisms offer further insights into the kinematics of these faults. Offshore Fethiye, two M_w 6.8 and 7.2 earthquakes in 1957 and a M_w 6.2 event in 2012 all have strike-slip mechanisms with NE-trending sinistral nodal planes (Figure 1b). However, depths of the 1957 earthquakes are poorly constrained and Howell et al. (2017) suggested that they occurred within subducting Nubian rather than overriding Anatolian lithosphere. The 2012 earthquake is better constrained through waveform modelling by Howell et al. (2017) and Görgün et al. (2014), confirming that it ruptured the Nubian plate at $\sim$30 km depth.

Otherwise, most well-studied earthquakes along the Fethiye-Burdur trend have involved crustal normal faulting of a variety of orientations. Largest amongst these were destructive earthquakes at Burdur in 1971 (M_w 6.0), Dinar in 1995 (M_w 6.5) and Sultandağı-Çay in 2000–2002 (earthquakes of M_w 6.0, 6.4 and 5.8), the focal mechanisms of which are plotted on Figure 1b. Using teleseismic body-waveform modelling, Taymaz & Price (1992) demonstrated that the 1971 Burdur earthquake involved normal slip and tentatively attributed it to the NW-dipping Hacılar fault. Wright et al. (1999) used InSAR to map normal slip along the SW-dipping Dinar fault in the 1995 Dinar earthquake, while Koçyiğit & Özacar (2003) and Aksarı et al. (2010) described how the 2000–2002 Sultandağı-Çay (Afyon) sequence involved NE-, N-, and NW-dipping normal faults in the Akşehir-Afyon graben. Finally, numerous smaller events (not shown in Figure 1b) have been modelled using regional waveforms. Över et al. (2010, 2013b, 2016) revealed a predominance of E–W normal faulting near Çameli, NE–SW normal faulting near Burdur, and N–S normal faulting within the interior Isparta angle, while Irmak (2013) determined a mixture of normal and strike-slip faulting in the Denizli region (Figure 1b).

2.3 Satellite geodesy

Global Navigation Satellite Systems (GNSS) geodesy has played an important role in arguments both for and against the FBFZ. The earliest regional GNSS studies revealed that sites along Turkey's Aegean coastline move ∼15–20 mm/yr more rapidly southwestwards than those along its Mediterranean coastline, and attributed this differential motion to left-lateral slip along the FBFZ (Eyidogan & Barka 1996; Barka & Reilinger 1997; Reilinger et al. 1997). However, these inferences were based on sparse campaign sites, with only fifteen situated within the footprint of Figure 1b. Since then, instalment of continuous GNSS stations has progressively densified this coverage (Reilinger et al. 2006; Aktug et al. 2009; Nocquet 2012; Tiryakioğlu et al. 2013), resulting in the velocities shown in Figure 2a–b which combine data from all of the earlier studies (Howell et al. 2017).

Using an elastic block model with boundaries assigned to the edges of a rigid Isparta angle, Reilinger et al. (2006) inverted the GNSS velocities to yield ∼3 mm/yr of sinistral slip and ∼4 mm/yr of shortening along the southwestern FBFZ with a switch to ∼11 mm/yr of dextral slip and ∼1 mm/yr of extension along the northeastern FBFZ. Using a similar approach but incorporating new GNSS data and slightly modified block boundaries, Tiryakioğlu et al. (2013) estimated ∼5 mm/yr of sinistral slip and ∼1 mm/yr of extension along the southwestern FBFZ, and ∼4 mm/yr each of dextral slip and extension along the northeastern FBFZ (Figure 2c). Both models also indicate ∼3–4 mm/yr of sinistral transtension along the eastern boundary of the Isparta angle, allowing for separation of the Isparta block from Anatolia. The switch from dextral to sinistral slip along the southwestern FBFZ, coupled with rapid (∼10–18 mm/yr) transtension along the Gediz graben, allows for even faster separation from Anatolia of a Menderes-Gökova block. Another shared feature is a block boundary linking the southern tip of the FBFZ with the eastern Hellenic arc and characterized by rapid (∼14–23 mm/yr) sinistral transpression (Figure 2c).

Aktug et al. (2009) took a markedly different approach, converting GNSS velocities into strain and rotation rate fields rather than inverting them for slip rates on pre-determined block boundaries. For significant strike-slip faulting to occur, the horizontal strain-rate tensor should exhibit extensional and shortening principal axes of similar magnitude. Instead, Aktug et al. (2009) found that throughout southwestern Turkey, the largest principal axes are extensional. They are oriented ∼N–S in the Büyük Menderes and Gediz graben northwest of the Fethiye-Burdur trend, but rotate to ∼E–W in the Isparta angle interior. Applying a similar strategy with additional data, Howell et al. (2017) determined that in the region of lacustrine basins known colloquially as the Lake District, there are *two* extensional principal axes of roughly equal magnitude, implying radial divergence (Figure 2d). Further south, their model predicts uniaxial extension accompanied by counterclockwise vertical axis rotations in the area around Fethiye.

3 DATA AND METHODS

3.1 InSAR observations and modelling

We used European Space Agency Sentinel-1 synthetic aperture radar interferograms and elastic dislocation modelling to characterize faulting in the 2017 Arıcılar and 2019 Acıpayam and Bozkurt earthquakes. For each event we used GAMMA software to construct short (6 or 12 day) coseismic interferograms on ascending track 58A and descending track 138D, choosing in each case the earliest available post-event scene in order to minimize the contribution from postseismic deformation. For the Arıcılar earthquake, we added a third interferogram from ascending track 131A; no Sentinel-1 scenes were captured between the two earthquakes, and so each interferogram captures the coseismic deformation of both events. Radar incidence angles are between 31° and 43° at the Arıcılar epicenter and between 36° and 38° at both the Acıpayam and Bozkurt epicenters.

To model the interferograms we followed the routine procedures of Wright et al. (2003), which have been deployed on several other modern earthquakes across Turkey (Taymaz et al. 2007; Elliott et al. 2013; Karasözen et al. 2016, 2018; Pousse-Beltran et al. 2020). We first downsampled the unwrapped interferograms using a Quadtree algorithm (Jónsson et al. 2002) and then solved for the fault plane parameters that minimize differences between these datapoints and synthetic displacements calculated for a rectangular fault plane embedded within an elastic half-space (Okada 1985). For the half-space, we chose Lamé parameters $\mu = 3.2 \times 10^{10}$ Pa and Poisson ratio 0.25, consistent with the velocity structure obtained and applied elsewhere in this study. We inverted for fault strike, dip, rake, uniform slip, center point, length, and top and bottom depths, as well as linear N–S and E–W orbital ramps and the zero displacement level, and obtained a global minimum misfit by using Powell's algorithm with multiple Monte Carlo restarts (Press et al. 1992; Clarke et al. 1997; Wright et al. 1999). Results are tabulated in Supplementary Table S1. Based on InSAR studies of other earthquakes of similar magnitude and depth, we can expect model uncertainties of up to $\sim$5° in strike and $\sim$10° in dip and rake for these uniform slip solutions (e.g. Taymaz et al. 2007; Roustaei et al. 2010; Elliott et al. 2013; Nissen et al. 2019).

Next, we separately solved for the slip distributions on these model faults planes by extending them along strike and up- and down-dip, subdividing them into 1 km $\times$ 1 km subfaults, and applying a Laplacian operator to force realistic slip gradients between neighboring patches (Wright et al. 2003). The 1 km subfault dimension was selected in order to help fit InSAR displacements close to any potential near-surface slip, but we recognize that for earthquakes of this size, slip model spatial resolution at depths of several kilometers is likely to be only $\sim$2–5 km (e.g. Elliott et al. 2015). Results are given in Supplementary Tables S2–S6 and have also been posted to the SRCMOD database (Mai & Thingbaijam (2014); see Data Availability).

3.2 Teleseismic body waveform modelling

We used long-period teleseismic body waveform modelling as an independent check on the source mechanisms and depths of the M_w 5.6 Acıpayam and M_w 5.9 Bozkurt mainshocks. By accounting for direct *P* and *S* waves and their surface-reflected depth phases *pP*, *sP* and *sS*, this method can resolve centroid depths of large ($M_w \geq \sim$5.5) earthquakes to within ∼3–4 km, a marked improvement on automated, global catalogs which often fix the depths of upper crustal events *a priori* (Molnar & Lyon-Caen 1989; Taymaz et al. 1990, 1991; Maggi et al. 2002; Wimpenny & Watson 2021). Uncertainties in strike, dip, and rake are typically estimated as ∼15°, ∼5°, and ∼15°, respectively.

We followed the procedures outlined by Molnar & Lyon-Caen (1989), in common with several other regional earthquake studies (e.g. Taymaz et al. 1991; Kiratzi & Louvari 2003; Benetatos et al. 2004; Shaw & Jackson 2010; Yolsal-Çevikbilen et al. 2014; Howell et al. 2017). For both events, we first selected waveforms recorded at distances of 30–80° — avoiding complications from the core — and then filtered them using a 15–100 second bandpass, which allows the earthquakes to be treated as simple point sources. We then used the MT5 version (Zwick et al. 1994) of the weighted least squares algorithm of McCaffrey & Abers (1988) and McCaffrey et al. (1991) to solve for the minimum misfit strike, dip, rake, centroid depth, seismic moment and source-time function of each event. These are found by minimizing residuals between observed *P* and *SH* waveforms and synthetic seismograms computed using *P*, *pP*, *sP*, *S* and *sS* phases of a point souce embedded within an elastic half-space. We chose V_P as 6.0 km/s, V_S as 3.5 km/s, and density as 2700 kg/m^3, consistent with regional constraints (see Section 3.4). For the observed *P* and *SH* waveforms, we used 30 second vertical component seismograms and 40 second transverse component seismograms, respectively. The synthetic waveforms were adjusted to match *P* and *S* arrival times picked from broadband records, and weighted by azimuthal density in the inversion.

3.3 Regional waveform modelling

We used regional waveform modelling to estimate moment tensors for thirty-six earthquakes in the 2017 Arıcılar and 2019 Acıpayam and Bozkurt sequences. Having larger signal-to-noise than teleseismic waveforms, regional waveforms permitted assessment of far smaller earthquakes, down to M_w 3.5 in this study.

We assessed around fifty earthquakes, presenting here only the thirty-six that met strict quality criteria and discarding the remainder. For each event, we gathered waveform data recorded over the distance range 50–200 km by stations belonging to several regional networks listed in the Acknowledgements. In rare instances, where a more distant station exhibiting favourable signal-to-noise could help fill a pronounced azimuthal gap, stations as far as 300 km were also included. The preferred frequency band for the inversion was selected after a careful analysis of the signal-to-noise ratio and station epicentral distances, and Green's functions were estimated for our own regional velocity model (Section 3.4) using the discrete wavenumber method of Bouchon (1981) and Coutant (1989). We then used the iterative deconvolution inversion method of Kikuchi & Kanamori (1991), implemented in the ISOLA software package (Sokos & Zahradník 2008; Zahradník & Sokos 2018), to solve for the best point source representation of each earthquake. We used the quality and variance reduction criteria detailed in the caption to Supplementary Table S7 to select the 36 robust solutions (Sokos & Zahradník 2013), and performed additional jack-knife tests (removing one station, re-inverting the waveforms, and comparing results) to corroborate the stability of each solution. We obtained $>$90% double-couple solutions for half of the earthquakes and majority double-couple solutions for all but one of them, lending further confidence in our results. We present here the best double-couple solutions.

Previous regional waveform modelling studies indicate that minimum misfit centroid depths can vary according to the station configurations, velocity models, and frequency bands used in the inversion (e.g. Zahradnik et al. 2008; Haddad et al. 2020). Accordingly, for a few of the critical, larger events analyzed, we repeated the inversion using perturbations to these parameters — including three alternative regional velocity models (Kalafat et al. 1987; Akyol et al. 2006; Brüstle 2013) — from which we estimated centroid depth uncertainties of $\sim$1–2 km. However, the smaller events studied here are likely to have greater uncertainties, perhaps up to around 5 km (Herman et al. 2014).

3.4 Calibrated hypocenter relocations

We used local, regional and teleseismic arrival times to relocate hypocenters of the 2017 Arıcılar and 2019 Acıpayam and Bozkurt sequences and earlier instrumental events from across southwestern Turkey. We selected 659 well-recorded earthquakes for our analysis, collating phase arrival times from the global International Seismological Centre (ISC) bulletin and from regional archives listed in the Acknowledgements. The selected events span from 1958 to August 2019 inclusive; those prior to the 1990s are all larger than m_b 4 while the 2017–2019 sequences include events as small as M_L 2. Since they cover an area larger than that typically covered in a single relocation, we separated the selected events into distinct geographic clusters, relocated each in turn, and collated the results (e.g. Karasözen et al. 2019; Pousse-Beltran et al. 2020). Two smaller clusters focus on the Acıpayam and Bozkurt sequences, and three larger ones are centered approximately upon Çameli in the southern study area, Burdur in the north, and Beyşehir in the east (Figure 3a).

Each cluster was relocated using the Hypocentroidal Decomposition (HD) method (Jordan & Sverdrup 1981) as implemented in the *mloc* program (Bergman & Solomon 1990; Walker et al. 2011). The HD algorithm divides the relocation procedure into two distinct inverse problems that each utilize customized phase arrival time data (e.g. Karasözen et al. 2016, 2018). The first step uses arrival times of all phases recorded at all distances to determine cluster vectors that relate the locations and origin times of each individual event with respect to the geometrical mean of all events, the hypocentroid. The second step uses direct *Pg* and *Sg* phases at epicentral distances $<2°$ — at which biases from unknown velocity structure are minimal — to establish the absolute location and origin time of the hypocentroid. The cluster vectors, added to the absolute hypocentroid, yield the calibrated coordinates of all events (meaning those in which biases from unknown earth structure are minimized): latitude, longitude, focal depth, origin time, and their uncertainties. The HD method can solve for focal depth as a free parameter if all events in the cluster have near-distance readings; around one third of the 659 relocated earthquakes were determined in this way, (including all of those in the Acıpayam and Bozkurt clusters). For most of the remainder, we set the depths manually by minimizing the residuals at close-in stations. For the final 100 events, focal depths were fixed to a default value of 10 km for the Çameli cluster and 15 km for the Burdur and Beyşehir clusters. Experiments on other HD clusters show that changing this default depth by $<$15 km has negligible impact on epicenter accuracy (Ghods et al. 2012; Karasözen et al. 2016).

By analyzing fits to *Pg* and *Sg* at the closest stations and *Pn* and *Sn* at distances of up to $\sim$8°, we settled upon a two-layered crustal velocity model with V_P 5.7 km/s and V_S 3.25 km/s for the upper 20 km and V_P 6.2 km/s and V_S 3.6 km/s from 20 km to the Moho at 40 km. Below the Moho, we used velocities from the *ak135* 1-D Earth model (Kennett et al. 1995). The relocation procedure eliminates systematic biases of up to $\sim$0.5 sec and $\sim$1.5 sec in *Pg* and *Sg* residual travel times, respectively, and reduces their root mean square errors from starting values of $\sim$1–2 sec down to $\sim$0.3–0.6 sec. Resulting, calibrated hypocenters are summarized in Supplementary Table S8 and we have posted detailed information on each cluster — such as arrival time compilations, station coordinates and calibration raypaths, velocity models, travel time residual plots, focal depth histograms, and epicentral uncertainty maps — to the Global Catalog of Calibrated Earthquake Locations database (Benz (2021); see Data Availability).

Epicenters have typical uncertainties of $\sim$1–2 km in latitude and longitude. Focal depth accuracy depends strongly on the availability of close-in stations, meaning those at epicentral distances less than $\sim$1–2 times the focal depth (e.g. Gomberg et al. 1990). In two previous studies of ours in neighbouring regions of western Turkey, we estimated these uncertainties at $\sim$2 km where close-in stations are available and $\sim$5 km where they are not (Karasözen et al. 2016, 2018). This marks a significant improvement on the relocated ISC-EHB catalogue, whose focal depth uncertainties have been estimated at $\sim$10–15 km (Engdahl et al. 2006). However, a comparison between our calibrated focal depths and centroid depths from regional waveform modelling reveals the former to be on average several kilometers deeper, with respective means of $\sim$8 km and $\sim$14 km (Supplementary Figure S1). This discrepancy holds for individual seismic sequences and is consistent across three orders of magnitude (M_w 3–6). It also mimics patterns observed elsewhere in western Turkey (Karasözen et al. 2016, 2018; Mutlu 2020) and in similarly well-instrumented regions of Alaska (Gaudreau et al. 2019) and Israel (Haddad et al. 2020). Our interpretation is that for most of the events analyzed, calibrated relocations provide an *upper bound* on focal depth while regional waveform modelling is better at resolving the shallowest earthquake depths.

3.5 Regional compilation of well-located earthquake focal mechanisms

Lastly, we compiled a regional catalogue of well-located earthquake focal mechanisms by combining our own results with source parameters from the literature. We found a total of 299 earthquake focal mechanisms spanning the interval 1955–August 2019 across the region shown in Figure 1b; the full catalogue, with references, is given in Supplementary Table S9. Of the larger events (greater than $M_w \sim$5), fifteen mechanisms were estimated using first motion polarities, thirty-six using teleseismic long-period body waveform modelling, and sixty-five were determined by the Global Centroid Moment Tensor (GCMT) project. In addition, 183 smaller events (M_w 3–5) were calculated using regional waveform modelling or first motions (mostly the former), but these go back only as far as 2001, around the time that station coverage across Turkey started to improve markedly. Of the 299 focal mechanism events, 241 have hypocenters determined from calibrated relocations, either in this study or by Karasözen et al. (2016, 2018). Most of the remainder are offshore earthquakes characterized by large azimuthal gaps at regional distances, making their precise relocation difficult. For these earthquakes, we choose the best available hypocenter from the ISC where possible: in most cases, we took the parameters listed in the relocated ISC-EHB catalogue (Engdahl et al. 1998; Weston et al. 2018). The final compilation of earthquakes is plotted in Figure 3b and described in Sections 4 and 5.

4 RESULTS PART I — THE SOUTHERN ISPARTA ANGLE

We first consider patterns of seismicity within the region covered by our Çameli cluster, south of $\sim$37.25° N and extending from the Gökova graben in the west across the Bey mountains in the east (Figure 3a). The relocated seismicity is broadly distributed and focal depths range from 7 km to 18 km with the greatest concentration at 10–14 km. The available earthquake focal mechanisms indicate a prevalence of normal faulting (Figure 3b). Most of those in the Bey mountains — largely regional waveform models from Över et al. (2016) — have $\sim$N–S-oriented nodal planes, consistent with trends of active normal faults mapped by Glover & Robertson (1998) in and around the Aksu basin. Several of the events have strike-slip components but few are dominantly strike-slip, and those which are do not have consistent nodal plane orientations.

The greatest concentration of earthquakes in the southern Isparta angle is situated between Fethiye, Muğla and Çameli, at the southwestern end of the Fethiye-Burdur trend (Figure 4). Here, the fifteen moderate magnitude earthquakes (up to M_w 5.4) with assigned focal mechanisms almost exclusively involve ESE–WNW-oriented normal faulting. Only one, relatively minor earthquake — a M_w 4.5 aftershock within the 2007 sequence south of Çameli — has a predominantly strike-slip mechanism, with NE-trending dextral and NW-trending sinistral nodal planes (Över et al. 2010). Otherwise, nodal planes match the orientations of an array of discontinuous, $\sim$ESE-trending faults mapped by Elitez & Yaltırak (2014) and coined the Gökova-Yeşilüzümlü Fault Zone by Hall et al. (2014) (Figure 4). They ascribed it a sinistral-transtensional slip sense, but the earthquake focal mechanisms — whose relocated epicenters lie $\sim$10–20 km to the north — indicate predominantly normal motions. The faults that hosted these earthquakes appear to lack any clear topographic expression and can be inferred to be structurally-immature, by which we mean that they have yet to accommodate appreciable cumulative slip. This characteristic is exemplified by the 2017 Arıcılar earthquake, described in Section 4.1.

The longer and more topographically prominent faults in the area mostly follow northeasterly trends (Alçiçek et al. 2006; Alçiçek 2007; Elitez & Yaltırak 2014; Elitez et al. 2017), but the few relocated earthquakes along these structures are too small for robust focal mechanisms and so we cannot offer further insight into their kinematics. These NE-trending faults are discussed further in Section 6.1.

4.1 The 24 November 2017 M_w 5.3 Arıcılar earthquake

This event struck the mountainous region east of Muğla (in the western part of Figure 4), very close to the small hamlet of Arıcılar after which we have named it. A M_w 5.1 foreshock struck at 20:22 UTC (23:22 local time) on 22 November 2017 and is associated with peak intensities of V (KOERI). The M_w 5.3 mainshock occurred at 21:49 UTC on 24 November 2017 (at 00:49 on 25 November 2017, local time) and was felt at both Muğla and Fethiye according to responses to the United States Geological Survey (USGS) "Did You Feel It?" questionnaire. To our best knowledge, neither earthquake caused significant damage.

All of the available InSAR imagery captures both the foreshock and mainshock. Ascending and descending coseismic interferograms each exhibit an E–W-oriented, elliptical fringe pattern with peak line-of-sight displacements of $\sim$11–14 cm (Figure 5, left column). There is an area of pronounced phase decorrelation centered on the northern side of the deformation ellipse where the fringes are most closely spaced. Observed displacements were best reproduced by normal slip on a S-dipping model fault that extends from the surface to $\sim$4 km depth (Figure 5, center and right columns; Figure 6; Table 1). We explored but rejected an alternative, N-dipping model geometry on the basis that it produced tighter fringes along the south side of the deformation ellipse, rather than along the north side as observed (Supplementary Figure S2 and Table S1).

Relocated foreshock and mainshock epicenters suggest that both nucleated near the base of the N-dipping slip patch (Figure 6). Their combined seismological moments approximate the InSAR model moment, suggesting that both contributed to the observed surface deformation. Model slip peaks at $\sim$30–40 cm at $\sim$2 km depth, and a few centimeters of model slip reaches the surface over a distance of 4 km and close to the zone of InSAR phase decorrelation, suggesting that a small surface rupture may have occurred (Figure 6b). Very shallow coseismic slip is corroborated by our regional moment tensor centroid depths of $\sim$1–2 km (Table 1), which additional depth resolution tests confirmed as being robust. Such shallow confinement of rupture has been observed in a few other continental earthquakes in the Mediterranean and Middle East regions (Savidge et al. 2019; Ritz et al. 2020; Elias et al. 2021).

The causative fault is not evident in the topography and was not known prior to the earthquake (Figure 6a). However, it is only a few kilometers along strike from — and only $\sim$20° oblique to — the easternmost mapped extent of the SSW-dipping Muğla normal fault, which has a similar geological slip vector to that of our InSAR model (Howell et al. 2017). This implies that the 2017 earthquakes ruptured an eastern continuation of the Muğla fault zone.

5 RESULTS PART II — THE NORTHERN ISPARTA ANGLE

We next consider patterns of seismicity north of $\sim$37.25° N in the regions covered by our Beyşehir, Burdur, Acıpayam and Bozkurt clusters (Figure 3a). The relocated seismicity is broadly distributed with focal depths concentrated in the range 10–19 km. The available earthquake focal mechanisms indicate a prevalence of normal faulting with a wide diversity of orientations (Figure 3b). This diversity is especially evident along the northeastern Fethiye-Burdur trend, from Acıpayam basin in the southwest to the Akşehir-Afyon graben in the northeast. This area exhibits a mix of NW-, W- and SW-trending normal mechanisms.

Regarding the purported FBFZ, several earthquakes with well-constrained focal mechanisms are colocated with NE-trending faults and therefore warrant closer scrutiny. These events are concentrated in the Burdur region (Figure 7) and the largest of them, the 12 May 1971 M_w 6.0 Burdur earthquake, is assessed separately in Section 5.3. Two earthquakes with relocated hypocenters within the Tefenni basin (in the southern part of Figure 7) are of particular interest, since Aksoy & Aksarı (2016) mapped several NE-striking sinistral strike-slip faults in this area. The larger of the two — a M_w 5.5 earthquake on 30 January 1964 near Karamanlı — has a first motions mechanism consistent with steep, SW-dipping sinistral-normal faulting (Canitez & Üçer 1967) and may have ruptured one of a number of NW-striking faults mapped in this area. The smaller of the two — a M_w 3.6 event on 21 July 2019 — is colocated with a NE–trending fault, but our regional waveform model indicates predominantly normal motion. $\sim$20 km west of the Tefenni basin, a M_w 4.6 earthquake on 4 December 2009 with a normal mechanism (Över et al. 2013b) is relocated to the northern end of the NE-trending Çameli fault, described by Elitez & Yaltırak (2016) and Emre et al. (2018) as sinistral or sinistral transtensional. This reinforces the competing interpretation of Alçiçek et al. (2006) and Özkaptan et al. (2018) that the Çameli fault accommodates normal slip, and is also consistent with a recent paleoseismic study that showed predominantly normal motion on the nearby, parallel Acıpayam fault (Kürçer et al. 2016).

There are only a very few scattered strike-slip events, most of them located west of the main Fethiye-Burdur trend in the Denizli region (Figure 3b and NW corner of Figure 7) and all with small to moderate magnitudes. Elsewhere, a m_b 5.3 earthquake on 9 September 1971, which we relocated to the Korkuteli basin (SE corner of Figure 7), was previously assigned a pure strike-slip mechanism (Yılmaztürk & Burton 1999) and has been used as evidence for a left-lateral FBFZ (Hall et al. 2009). However, Yılmaztürk & Burton (1999) only modelled ten teleseismic *P* waveforms and acknowledged large residuals at some of these stations, which is suggestive of large uncertainties in the mechanism. Moreover, their centroid depth of 34 km is inconsistent with our focal depth of 15 km and with other regional focal depths. For these reasons, we consider this event to have questionable source parameters and do not include it in our focal mechanism database.

5.1 The 20 March 2019 M_w 5.6 Acıpayam earthquake

This M_w 5.6 earthquake struck the Acıpayam basin (SW corner of Figure 7) on 20 March 2019 at 06:34 UTC and 09:34 local time. According to the Kandilli Observatory and Earthquake Research Institute (KOERI), Modified Mercalli intensities reached VI in the eastern basin, where several rural homes were completely destroyed, and V in the town of Acıpayam in the western basin, where three people were injured by falling debris. The USGS documents “Did You Feel It?” felt reports as far away as İzmir, ∼240 km west of the epicenter.

InSAR data reveal a NW–SE-oriented elliptical fringe pattern with line-of-sight displacements of up to ∼5 cm away from the satellite (Figure 8a, left column). Our elastic dislocation modelling best reproduced the observed ground deformation with normal slip on a buried, moderately (54°) NE-dipping model fault that projects to the surface within the flat, central Acıpayam basin (Figure 8a, center and right columns; Figure 9a; and Table 1). Our relocated hypocenter lies just down-dip of the southeastern extent of model slip patch, suggesting that the mainshock rupture propagated upwards and unilaterally towards the NW (Figure 9a). An alternative, SW-dipping model fault reproduced the data nearly as well, but we consider this geometry unlikely on the basis that the relocated hypocenter would be located up-dip of the main slip area (Supplementary Figure S3). On our preferred, NE-dipping model fault, slip is restricted to a depth range of ∼4–9 km with peak slip of ∼0.3 m at ∼6 km depth (Figure 9b), matching the minimum misfit centroid depth from teleseismic body waveform modelling (Figure 10) and only slightly shallower than the ∼7 km centroid depth estimated using regional waveforms (Table 1). Finally, we note that our preferred source parameters are in good agreement with alternative InSAR-derived slip models by Yang et al. (2020) and Elliott et al. (2020), with discrepancies of 10° or less in strike, dip and rake, and near-identical slip depth ranges.

The mainshock was preceded ∼5 hours earlier by a moderate (M_w 3.7) foreshock, located ∼1 km to the SE and with a similar normal mechanism (Figure 9a and Supplementary Table S7). An abundant aftershock sequence includes 193 earthquakes with sufficient station picks for precise relocation, of which twenty-three were sufficiently large (M_w 3.5–5.1) that we could obtain robust focal mechanisms and centroid depths. The aftershocks form a diffuse distribution, with several colocated with the mainshock slip region but others lying well away from it. Centroid depths range from 3–15 km, with the greatest concentration at 4–5 km, but likely uncertainties of up to a few kilometers make it difficult to ascertain whether the colocated events lie on, or off (below or above), the mainshock fault plane. Southern aftershocks — including a cluster around the southern end of the mainshock slip region — tend to have normal mechanisms similarly oriented to that of the mainshock and so might plausibly lie on the same fault plane. Northern aftershocks, on the other hand, involve normal faulting with a greater diversity of orientations including a few orthogonal to the main fault plane. The northern aftershocks also include a few oblique slip events and a single strike-slip earthquake (a M_w 3.6 event with NE-oriented dextral and NW-oriented sinistral nodal planes).

The mainshock fault is highly oblique to the sinistral–normal Acıpayam fault in the southern Acıpayam basin (Kürçer et al. 2016; Emre et al. 2018) and somewhat oblique to a number of unnamed, N–S-trending normal faults portrayed across the eastern basin by Alçiçek et al. (2006) and Elitez & Yaltırak (2016) (Figure 9a). However, the mainshock fault itself was not recognized prior to the 2019 earthquake and there are no clear fault scarps visible along its surface projection, even with the aid of high-resolution topographic imagery (Elliott et al. 2020). This suggests either that shallow extension is accommodated elsewhere — perhaps by distributed deformation — or that the fault is structurally immature. The inference of structural immaturity is consistent with our observation of diffuse aftershock seismicity, much of it presumably on structures subsidiary to the mainshock fault (Powers & Jordan 2010; Pousse-Beltran et al. 2020; Perrin et al. 2021). Some of the N–S-oriented aftershocks, including the largest (M_w 5.1) on 31 March 2019, may have occurred on the faults mapped by Alçiçek et al. (2006) and Elitez & Yaltırak (2016). However, none of the aftershocks are colocated with the larger Acıpayam fault and so we cannot provide new information on its kinematics.

5.2 The 8 August 2019 M_w 5.9 Bozkurt earthquake

This M_w 5.9 earthquake struck near the town of Bozkurt in the western Acıgöl basin (in the northern part of Figure 7) on 8 August 2019 at 11:25 UTC and 14:25 local time. Peak intensities of VI were recorded in and around the town of Bozkurt (KOERI) and $\sim$23 people were injured and more than 100 houses heavily damaged. The earthquake was felt at İzmir, $\sim$230 km to the west, and Konya, $\sim$250 km to the east (USGS “Did You Feel It?”).

Radar interferograms exhibit a circular fringe pattern centered on Maymundağ mountain, north of Acıgöl basin (Figure 8b, left column). The pattern is clearest in the descending interferogram, where peak line-of-sight displacements are $\sim$4 cm away from the satellite. We replicated the observed deformation most closely with normal slip on a buried, $\sim$N- or $\sim$S-dipping model fault. We favour the N-dipping model (Figure 9c, center and right columns) since its parameters are in much closer agreement with our teleseismic body waveform focal mechanism (Figure 11; Table 1). For reference, the alternative S-dipping model is plotted in Supplementary Figure S4. Though the InSAR model strike is poorly resolved due to the circular deformation pattern, our minimum misfit value of 270° lies centrally within the range of seismological estimates (254°–289°). Our relocated hypocenter lies at the western edge of the modelled fault slip, suggesting unilateral, eastward rupture. Model fault slip occurs at depths of $\sim$6–10 km with peak slip of $\sim$0.6 m at $\sim$8.5 km (Figure 9d). Our teleseismic waveform model centroid depth is somewhat deeper at $\sim$12 km, though we find similar waveform misfits across the centroid depth range 9–14 km. Our minimum misfit centroid depth from regional waveform modelling lies near the shallow end of this range, at $\sim$10 km (Table 1).

A M_w 4.1 foreshock and six M_w 3.6–4.0 aftershocks were sufficiently well-recorded for regional waveform modelling, and seven smaller aftershocks could also be precisely relocated (Figure 9c). The larger events involved predominantly normal faulting mechanisms — mostly oriented $\sim$E–W except for one which was oriented $\sim$N–S — at centroid depths of 5–11 km. Several of the aftershocks are located close to the up-dip edge of the InSAR-derived model slip distribution, though the limited depth resolution precludes any firm association or interpretation.

The surface projection of our model fault aligns closely with a mapped, N-facing scarp in the southern part of Acıgöl basin, $\sim$3 km north of the main, rangefront-forming Acıgöl fault (Figure 8b). Topographic profiling indicates that the scarp is around 5–10 m high. Its involvement in the August 2019 sequence may indicate a basinward migration or reorganization of the Acıgöl fault zone that helps straighten a curved embayment in the southern basin margin. However, only the deep portion of this fault ruptured in the 2019 Bozkurt earthquake. We tentatively suggest that the S-dipping Maymundağ fault — which bounds the northern margin of the basin and which presumably abuts the N-dipping fault at depths of several kilometers — may have formed a structural barrier across which slip in the Bozkurt earthquake failed to propagate. This is similar to inferences made on the depth extents of certain reverse faulting earthquakes (Elliott et al. 2011, 2013; Savidge et al. 2019).

5.3 The 12 May 1971 M_w 6.0 Burdur earthquake revisited

The destructive 12 May 1971 M_w 6.0 Burdur earthquake caused extensive damage to villages at the southern end of Lake Burdur (in the eastern part of Figure 7) and killed 57 people. Teleseismic waveform modelling of the mainshock resolved two distinct sub-events separated by 9 seconds, each exhibiting a predominantly normal mechanism with moderate dip angle (35–56°) SW- and NE-striking nodal planes and a centroid depth of 12 km (Taymaz & Price 1992). Two early aftershocks also have predominantly normal mechanisms, but with steeper (65° or 90°) NW-dipping nodal planes consistent with normal faulting downthrown on the NW side (McKenzie 1978; Taymaz & Price 1992). Documentation of primary surface rupturing is inconclusive, but cracks were observed along the SE margin of the lake, downthrown 20–30 cm to the NW. Collectively, these observations implied to Taymaz & Price (1992) that the NW-dipping Hacılar and Suludere faults — which form the clear topographic scarp along the SE margin of Burdur basin — were responsible for the 1971 earthquake, with the possible additional involvement of the Pınarbaşı fault in the northern Tefenni basin.

Our hypocentral relocations place the Burdur mainshock and largest two aftershocks close to Lake Salda, ∼30 km WSW of Lake Burdur (in the central part of Figure 7). Smaller relocated aftershocks form a broader distribution between Lake Salda in the WSW and the southern end of Lake Burdur in the ENE. The orientation of the aftershock cloud matches the strike of the mainshock nodal planes but its length of 30–40 km likely exceeds that of the M_w 6.0 mainshock fault plane based on scaling relations (Wells & Coppersmith 1994). The easternmost aftershocks are therefore likely to be situated some distance along strike from the mainshock rupture. Collectively, this suggests that the Burdur mainshock propagated unilaterally towards the ENE from its epicenter near Lake Salda, but that it terminated well short of the Hacılar and Suludere faults that were attributed to this earthquake by Taymaz & Price (1992). The heavy damage to villages at the southern end of Lake Burdur likely reflects this rupture directivity, while the cracks observed along the SE margin of the lake might reflect secondary deformation related to liquefaction or landsliding which was also observed in this area.

The Burdur mainshock faulting is therefore confined to the area between Salda and Yarışlı Lakes, which exhibits indistinct surface geomorphology and lacks mapped surface faulting. The tight clustering of the mainshock and two largest aftershocks coupled with their diversity of nodal plane dip angles suggests high structural complexity within the source region. These observations hint that the M_w 6.0 Burdur earthquake ruptured an immature fault with low cumulative slip, much like the 2017 M_w 5.3 Arıcılar, 2019 M_w 5.6 Acıpayam and M_w 5.9 Bozkurt earthquakes analyzed previously.

6 DISCUSSION

6.1 Kinematics of the deformation

The results outlined in Sections 4–5 enable a critical assessment of GNSS-derived kinematic models of regional deformation. We focus especially on those of Tiryakioğlu et al. (2013) and Howell et al. (2017), since they are based on the densest, published GNSS velocity fields (Figure 2).

Near Fethiye at the southwestern end of the Fethiye-Burdur trend, the predominance of ESE-trending normal faulting earthquake focal mechanisms contradicts GNSS-derived block models which show NE-trending sinistral (Tiryakioğlu et al. 2013) or even sinistral-transpressional (Reilinger et al. 2006) motions through this area. Instead, the focal mechanisms are in very good agreement with the GNSS strain rate field of Howell et al. (2017) which indicates NNE-SSW oriented extension. This calls into question the relative activity of the NE-trending faults, which are much clearer in the geomorphology, exhibit abundant normal and normal-sinistral slickensides on exposed fault planes (Alçiçek et al. 2006; Elitez & Yaltırak 2014; Howell et al. 2017; Özkaptan et al. 2018; Tosun et al. 2021), but appear poorly oriented with respect to the modern strain rate field for continued extension. The most prominent cluster of ESE–WNW-oriented normal faulting earthquakes — the 2007 sequence southwest of Çameli — even appears to cross-cut nearby NE-trending faults bounding the southern Çameli basin (Figure 4).

We can think of two possible ways to reconcile these observations. Firstly, counterclockwise vertical axis rotations may have acted to reorient the older faults, which are of Late Miocene age (Alçiçek et al. 2006; Elitez & Yaltırak 2016), into their current, kinematically-unfavourable positions. However, current counterclockwise rotation rates in this region are only $\sim$2–3°/Myr (Howell et al. (2017); Figure 2d) and paleomagnetic data indicate cumulative counterclockwise rotations of $\sim$11–15° since the Late Miocene (Kaymakcı et al. 2018). This is clearly insufficient to account fully for the roughly $\sim$60° difference in strike between the instrumental earthquake nodal planes and the largest faults. A second possibility is that there has been a recent change in the regional strain field, from NW–SE-directed extension to NNE–SSW extension. Fault kinematic and tectonostratigraphic data from the Çameli basin support such a change and constrain its timing to the late Quaternary (Alçiçek et al. 2006), and similar patterns are observed in the Eşen-Çay basin (ten Veen 2004; Över et al. 2013a). We speculate that the switch might be related to eastward propagation of the Gökova graben into the area (Tur et al. 2015) and/or to lateral gradients in gravitational potential energy introduced by rapid subsidence of the Rhodes basin since the middle Pliocene (Woodside et al. 2000; Hall et al. 2009) (Figure 1b).

In the Lake District along the northeastern Fethiye-Burdur trend, there is likewise no evidence from earthquake focal mechanisms for through-going strike-slip faulting as depicted in GNSS elastic block models (Reilinger et al. 2006; Tiryakioğlu et al. 2013). Instead, the mix of NW-, W- and SW-trending normal faulting mechanisms is broadly consistent with the smoothed GNSS strain rate field of Howell et al. (2017), which shows radial divergence in this area (Figure 2d). We consider it likely that the orthogonal normal faulting is partly responsible for the numerous lacustrine basins. We next consider the forces responsible for this unusual pattern of strain.

6.2 Dynamics of the deformation

Data from multiple sources indicate radial horizontal extension along the northeastern Fethiye-Burdur trend. We now discuss why this radial extension might occur. Processes that are thought to drive deformation in the Aegean and Anatolia include: (1) slab rollback in the Hellenic and Cyprus subduction zones, possibly associated with one or more tears in the down-going Nubian plate; (2) the Nubia-Arabia-Eurasia collision; and (3) contrasts in gravitational potential energy (GPE) between the eastern Mediterranean sea floor and the continental lithosphere of Greece and Turkey. Of this, it is unclear how much (if at all) subduction rollback or the Arabian-Eurasia collision influence observed present-day strains in SW Turkey, or whether a possible tear in the Nubian plate beneath the Fethiye-Burdur trend contributes to surface deformation. By contrast, it is almost certain that contrasts in GPE contribute significantly to surface deformation in southwestern Turkey, given the $\sim$4–6 km differences in elevation between the deep Rhodes and Antalya basins and the Bey mountains between Fethiye and Antalya. We now consider deformation in southwestern Turkey in the light of previously published models of GPE contrasts.

Özeren & Holt (2010) calculated the deviatoric stress field expected from GPE contrasts alone (without applying any compressional boundary condition). The regime in their model aligns very well with our smoothed strain-rate field in Figure 2d — although we note that the modelled stress field exhibits a strong dependence on modelled crustal thickness. Their model predicts a localized area of radial extensional stresses around Burdur, apparently caused by the superposed effects of two lateral gradients in GPE: (1) a NE–SW gradient between Burdur and the Rhodes Basin; and (2) a NW–SE gradient between Burdur and the Antalya basin. Both west and east of Burdur, the stress field predicts more uniaxial horizontal extension associated with each GPE gradient; radial horizontal extension is only expected in the region equidistant from the Rhodes and Antalya basins. Lateral variations in GPE are therefore sufficient to explain the large-scale pattern of surface deformation in southwestern Turkey, although it is hard to rule out contributions from other dynamic processes.

7 CONCLUSIONS

Our refined and expanded earthquake catalog for southwestern Turkey reveals no evidence for NE-trending, active strike-slip faults along the Fethiye-Burdur trend, as has previously been posited. Instead, the western limb of the Isparta angle is characterized by shallow normal faulting earthquakes, with a diversity of orientations in the north (across Turkey's Lake District), mostly N–S nodal planes in the east (in the Bey mountains), and ESE–WNW nodal planes in the southwest (near Fethiye and Çameli). In each case, fault orientations are consistent with the principal axes of the horizontal strain rate tensor calculated from regional GNSS velocities (Howell et al. 2017). We suggest that these kinematics are driven principally by lateral gradients in gravitational potential energy between the high Anatolian plateau and the deep Rhodes and Antalya basins.

Three earthquake sequences associated with clear InSAR signals provide additional information on how active faulting is manifest in the topography. The 2017 M_w 5.3 Arıcılar earthquake was unusually shallow, with slip confined to above $\sim$4 km depth; we do not know whether it ruptured to the surface. Its causative fault lies a few kilometers along strike of the mapped Muğla fault zone but appears indistinct in the topography. The 2019 M_w 5.6 Acıpayam earthquake involved buried slip at $\sim$4–9 km depth on a previously unrecognized fault with no discernible geomorphic expression. The 2019 M_w 5.9 Bozkurt earthquake was buried even deeper at $\sim$6–10 km, and its fault plane aligns with subtle (5–10 m-high) surface scarps that had previously been mapped. All three of these earthquakes can therefore be inferred to have ruptured structurally-immature (low cumulative slip) faults. Our relocation of the destructive 1971 M_w 6.0 Burdur earthquake and its aftershocks hints that this sequence also ruptured a structurally-immature fault zone with an indistinct expression in the topography. While the largest instrumental events along the Fethiye-Burdur trend — the 1914 Burdur (M_S 7.0), 1995 Dinar (M_w 6.5) and 2002 Çay (M_w 6.4) earthquakes — ruptured structurally-mature normal faults with clear surface expressions, our observations raise the spectre that damaging earthquakes of up to at least M_w 6 are also possible on faults that would prove difficult to identify beforehand.

ACKNOWLEDGMENTS

E. N. was supported by a Canada Research Chair and grants from the Natural Sciences and Engineering Research Council of Canada (NSERC Discovery Grant 2017-04029), the Canada Foundation for Innovation, and the BC Knowledge Development Fund. E. G. was funded through an Alexander Graham Bell Canada Graduate Scholarship from NSERC, and a Montalbano Scholars Fellowship and President's Research Scholarship, both from University of Victoria. E. S. was assisted by an Undergraduate Student Research Award from NSERC and a Jamie Cassels Undergraduate Research Award from the University of Victoria. We thank Eric Bergman for guidance in earthquake relocation with *mloc* and we are grateful for critical comments from two anonymous reviewers and the Editor Sidao Ni which greatly improved the manuscript.

Data Availability

Interferograms were constructed using Copernicus Sentinel-1 data (2017, 2019) available from https://scihub.copernicus.eu/. Corresponding interferograms are also available to download from the COMET LiCS database (Wright et al. 2016), which we exploited during our initial reconnaissance of the Acıpayam, Bozkurt and Arıcılar earthquakes. All InSAR-derived slip models for these events are tabulated in Supplementary Tables S2–S6 and our preferred models have also been uploaded to the SRCMOD database (http://equake-rc.info/srcmod/) (Mai & Thingbaijam 2014).

Teleseismic waveforms were accessed through IRIS Data Services, and specifically the IRIS Data Management Center (https://ds.iris.edu/ds/nodes/dmc/). which are funded through the Seismological Facilities for the Advancement of Geoscience and EarthScope (SAGE) Proposal of the National Science Foundation under Cooperative Agreement EAR-1261681. Regional waveforms were obtained from the Aristotle University Of Thessaloniki Seismological Network (1981) (https://doi.org/10.7914/SN/HT), the Disaster And Emergency Management Authority (1990) of Turkey (https://doi.org/10.7914/SN/TU), the Technological Educational Institute Of Crete (2006) (https://doi.org/10.7914/SN/HC), the Kandilli Observatory and Earthquake Research Institute, Boğaziçi University (1971) (https://doi.org/10.7914/SN/KO), and the National Observatory Of Athens, Institute Of Geodynamics (1997) (https://doi.org/10.7914/SN/HL). Arrival times were gathered from the Disaster And Emergency Management Authority (1990) of Turkey, the Kandilli Observatory and Earthquake Research Institute, Boğaziçi University (1971), the National Observatory Of Athens, Institute Of Geodynamics (1997), and the International Seismological Centre (ISC) Bulletin (https://doi.org/10.31905/D808B830).

Our full, calibrated relocation results are available through the Global Catalog of Calibrated Earthquake Locations (GCCEL) database (https://doi.org/10.5066/P95R8K8G) (Benz 2021). Additional location parameters were taken from the ISC's relocated ISC-EHB dataset (https://doi.org/10.31905/PY08W6S3) and their ISC-GEM Earthquake Catalogue (https://doi.org/10.31905/d808b825). We used focal mechanisms from the Global Centroid Moment Tensor project (https://www.globalcmt.org/); from the U.S. Geological Survey's Comprehensive Earthquake Catalog (https://earthquake.usgs.gov/data/comcat/); and from the GEOFON Data Centre (1993) of the GFZ German Research Centre for Geosciences (https://geofon.gfz-potsdam.de/) which are based on data from the GEOFON Extended Virtual Network (GEVN) partner networks. Complete references for these earthquake parametric data sources are given in Supplementary Table S9.

The ISOLA software can be downloaded from http://seismo.geology.upatras.gr/isola/ and *mloc* source code from https://seismo.com/mloc/source-code/. Other codes used in the paper will be shared upon reasonable request to the corresponding author. All figures in this paper were plotted using *Generic Mapping Tools* (Wessel et al. 2013).

REFERENCES

Aksarı, D., Karabulut, H., & Özalaybey, S., 2010. Stress interactions of three moderate size earthquakes in Afyon, southwestern Turkey, *Tectonophys.*, **485**(1), 141–153.

Aksoy, R. & Aksarı, S., 2016. Neogene-Quaternary evolution of the Tefenni basin on the Fethiye-Burdur fault zone, SW Anatolia-Turkey, *J. Asian Earth Sci.*, **118**, 137–148.

Aktug, B., Nocquet, J. M., Cingöz, A., Parsons, B., Erkan, Y., England, P., Lenk, O., Gürdal, M. A., Kilicoglu, A., Akdeniz, H., & Tekgül, A., 2009. Deformation of western Turkey from a combination of permanent and campaign GPS data: Limits to block-like behavior, *J. Geophys. Res.*, **114**.

Akyol, N., Zhu, L., Mitchell, B. J., Sözbilir, H., & Kekovalı, K., 2006. Crustal structure and local seismicity in western Anatolia, *Geophys. J. Int.*, **166**, 1259–1269.

Alçiçek, M. C., 2007. Tectonic development of an orogen-top rift recorded by its terrestrial sedimentation pattern: The Neogene Eșen Basin of southwestern Anatolia, Turkey, *Sed. Geol.*, **200**(1–2), 117–140.

Alçiçek, M. C., 2015. Comment on "The Fethiye–Burdur Fault Zone: A component of upper plate extension of the subduction transform edge propagator fault linking Hellenic and Cyprus Arcs, Eastern Mediterranean. Tectonophysics 635, 8099" by J. Hall, A.E. Aksu, İ. Elitez, C. Yaltırak, G. Çifçi, *Tectonophys.*, **664**, 1–4.

Alçiçek, M. C., Ten Veen, J. H., & Özkul, M., 2006. Neotectonic development of the Cameli Basin, southwestern Anatolia, Turkey, *Geol. Soc. London Spec. Publ.*, **260**(1), 591–611.

Alçiçek, M. C., Brogi, A., Capezzuoli, E., Liotta, D., & Meccheri, M., 2013. Superimposed basin formation during Neogene-Quaternary extensional tectonics in SW-Anatolia (Turkey): Insights from the kinematics of the Dinar Fault Zone, *Tectonophys.*, **608**, 713–727.

Ambraseys, N. N. & Jackson, J. A., 1998. Faulting associated with historical and recent earthquakes in the Eastern Mediterranean region, *Geophys. J. Int.*, **133**, 390–406.

Aristotle University Of Thessaloniki Seismological Network, 1981. Permanent Regional Seismological Network operated by the Aristotle University of Thessaloniki.

Barka, A. & Reilinger, R., 1997. Active tectonics of the Eastern Mediterranean region: deduced from GPS, neotectonic and seismicity data, *Annali di Geofisica*, **40**(3), 587–610.

Benetatos, C., Kiratzi, A., Papazachos, C., & Karakaisis, G., 2004. Focal mechanisms of shallow and intermediate depth earthquakes along the Hellenic Arc, *J. Geodynamics*, **37**, 253–296.

Benz, H. M., 2021. Global Catalog of Calibrated Earthquake Locations, https://doi.org/10.5066/P95R8K8G, U.S. Geological Survey data release.

Bergman, E. A. & Solomon, S. C., 1990. Earthquake swarms on the Mid-Atlantic Ridge — Products of magmatism or extensional tectonics?, *J. Geophys. Res.*, **95**, 4943–4965.

Bouchon, M., 1981. A simple method to calculate Green's functions for elastic layered media, *Bull. Seismol. Soc. Am.*, **71**(4), 959–971.

Brüstle, A., 2013. *Seismicity of the eastern Hellenic Subduction Zone*, doctoralthesis, Ruhr-Universität Bochum.

Canitez, N. & Üçer, S. B., 1967. Computer determinations for the fault-plane solutions in and near Anatolia, *Tectonophys.*, **4**(3), 235–244.

Clarke, P. J., Paradissis, D., Briole, P., England, P. C., Parsons, B. E., Billiris, H., Veis, G., & Ruegg, J.-C., 1997. Geodetic investigation of the 13 May 1995 Kozani-Grevena (Greece) earthquake, *Geophys. Res. Lett.*, **24**, 707–710.

Coutant, O., 1989. Program of numerical simulation AXITRA, Tech. rep., Université Joseph Fourier Grenoble, France.

Demircioğlu, M. B., Şeşetyan, K., Duman, T. Y., Can, T., Tekin, S., & Ergintav, S., 2018. A probabilistic seismic hazard assessment for the Turkish territory: part II—fault source and background seismicity model, *Bull. Earthquake Eng.*, **16**(8), 3399–3438.

Disaster And Emergency Management Authority, 1990. Turkish National Seismic Network.

Dumont, J. F., Poisson, A., & Şahinci, A., 1979. Sur l'existence de coulissements sénestres récents a l'extrémité orientale de l'arc égéen (sud-ouest de la Turquie), *C. R. Acad. Sci.*, **289**, 261–264.

Elias, P., Spingos, I., Kaviris, G., Karavias, A., Gatsios, T., Sakkas, V., & Parcharidis, I., 2021. Combined Geodetic and Seismological Study of the December 2020 Mw= 4.6 Thiva (Central Greece) Shallow Earthquake, *Applied Sciences*, **11**(13), 5947.

Elitez, İ. & Yaltırak, C., 2014. Miocene–Quaternary geodynamics of Çameli Basin, Burdur-Fethiye Shear Zone (SW Turkey), *Geol. Bull. Turk.*, **57**, 41–67.

Elitez, İ. & Yaltırak, C., 2016. Miocene to Quaternary tectonostratigraphic evolution of the middle section of the Burdur-Fethiye Shear Zone, south-western Turkey: Implications for the wide inter-plate shear zones, *Tectonophys.*, **690**, 336–354.

Elitez, I., Yaltırak, C., Hall, J., Aksu, A. E., & Çifçi, G., 2015. Reply to the comment by M.C. Alçiçek on "The Fethiye-Burdur Fault Zone: A component of upper plate extension of the subduction transform edge propagator fault linking Hellenic and Cyprus Arcs, Eastern Mediterranean," Tectonophysics, 635, 80-99, by J. Hall, A.E. Aksu, İ. Elitez, C. Yaltırak and G. Çifçi, *Tectonophys.*, **664**, 5–13.

Elitez, İ., Yaltırak, C., & Aktuğ, B., 2016. Extensional and compressional regime driven left-lateral shear in southwestern Anatolia (eastern Mediterranean): The Burdur-Fethiye Shear Zone, *Tectonophys.*, **688**, 26–35.

Elitez, İ., Yaltırak, C., Kürçer, A., Özdemir, E., & Güldoğan, Ç. U., 2017. A critical review of the Kibyra Fault (Burdur-Fethiye Shear Zone, SW Turkey), *Geodinamica Acta*, **29**(1), 91–102.

Elliott, J. R., Parsons, B., Jackson, J. A., Shan, X., Sloan, R. A., & Walker, R. T., 2011. Depth segmentation of the seismogenic continental crust: The 2008 and 2009 Qaidam earthquakes, *Geophys. Res. Lett.*, **38**.

Elliott, J. R., Copley, A. C., Holley, R., Scharer, K., & Parsons, B., 2013. The 2011 Mw 7.1 Van (Eastern

Turkey) earthquake, *J. Geophys. Res.*, **118**(4), 1619–1637.

Elliott, J. R., Bergman, E. A., Copley, A. C., Ghods, A. R., Nissen, E. K., Oveisi, B., Tatar, M., Walters, R. J., & Yamini-Fard, F., 2015. The 2013 Mw 6.2 Khaki-Shonbe (Iran) earthquake: Insights into seismic and aseismic shortening of the Zagros sedimentary cover, *Earth Space Sci.*, **2**(11), 435–471.

Elliott, J. R., de Michele, M., & Gupta, H. K., 2020. Earth Observation for Crustal Tectonics and Earthquake Hazards, *Surveys in Geophysics*, **41**(6), 1355–1389.

Emre, O., Duman, T. Y., Özalp, S., Şaroğlu, F., Olgun, c., Elmacı, H., & Çan, T., 2018. Active fault database of Turkey, *Bull. Earthquake Eng.*, **16**(8), 3229–3275.

Engdahl, E. R., van der Hilst, R. D., & Buland, R., 1998. Global teleseismic earthquake relocation from improved travel times and procedures for depth determination, *Bull. Seismol. Soc. Am.*, **88**, 722–743.

Engdahl, R. E., Jackson, J. A., Myers, S. C., Bergman, E. A., & Priestley, K., 2006. Relocation and assessment of seismicity in the Iran region, *Geophys. J. Int.*, **167**, 761–778.

England, P., Howell, A., Jackson, J., & Synolakis, C., 2015. Palaeotsunamis and tsunami hazards in the Eastern Mediterranean, *Phil. Trans. R. Soc. Lond. A*, **373**(2053), 20140374.

England, P., Houseman, G., & Nocquet, J.-M., 2016. Constraints from GPS measurements on the dynamics of deformation in Anatolia and the Aegean, *J. Geophys. Res.*, **121**(12), 8888–8916.

Eyidogan, H. & Barka, A., 1996. October 1, 1995 Dinar earthquake, western Turkey, *Terra Nova*, **8**, 479–485.

Gaudreau, É., Nissen, E. K., Bergman, E. A., Benz, H. M., Tan, F., & Karasözen, E., 2019. The August 2018 Kaktovik earthquakes: Active tectonics in northeastern Alaska revealed with InSAR and seismology, *Geophys. Res. Lett.*, **46**, 14,412–14,420.

GEOFON Data Centre, 1993. GEOFON Seismic Network.

Ghods, A., Rezapour, M., Bergman, E., Mortezanejad, G., & Talebian, M., 2012. Relocation of the 2006 Mw 6.1 Silakhour, Iran, Earthquake Sequence: Details of Fault Segmentation on the Main Recent Fault, *Bull. Seismol. Soc. Am.*, **102**, 398–416.

Glover, C. & Robertson, A., 1998. Neotectonic intersection of the Aegean and Cyprus tectonic arcs: extensional and strike-slip faulting in the Isparta Angle, SW Turkey, *Tectonophys.*, **298**(1), 103–132.

Gomberg, J. S., Shedlock, K. M., & Roecker, S. W., 1990. The effect of S-wave arrival times on the accuracy of hypocenter estimation, *Bull. Seismol. Soc. Am.*, **80**(6A), 1605–1628.

Görgün, E., Zang, A., Kalafat, D., & Kekovalı, K., 2014. The 10 June 2012 Fethiye M_w 6.0 aftershock sequence and its relation to the 24-25 April 1957 M_s 6.9-7.1 earthquakes in SW Anatolia, Turkey, *J. Asian Earth Sci.*, **93**, 102–112.

Gürer, A., Bayrak, M., & Gürer, Ö. F., 2004. Magnetotelluric images of the crust and mantle in the southwestern Taurides, Turkey, *Tectonophys.*, **391**, 109–120.

Haddad, A., Alcanie, M., Zahradník, J., Lazar, M., Antunes, V., Gasperini, L., Polonia, A., Mazzini, A.,

& Lupi, M., 2020. Tectonics of the Dead Sea Fault Driving the July 2018 Seismic Swarm in the Sea of Galilee (Lake Kinneret), Israel, *J. Geophys. Res.*, **125**(10).

Hall, J., Aksu, A. E., Yaltırak, C., & Winsor, J. D., 2009. Structural architecture of the Rhodes Basin: A deep depocentre that evolved since the Pliocene at the junction of Hellenic and Cyprus Arcs, eastern Mediterranean, *Marine. Geol.*, **258**(1–4), 1–23.

Hall, J., Aksu, A. E., Elitez, I., Yaltırak, C., & Çifçi, G., 2014. The Fethiye-Burdur Fault Zone: A component of upper plate extension of the subduction transform edge propagator fault linking Hellenic and Cyprus Arcs, Eastern Mediterranean, *Tectonophys.*, **635**, 80–99.

Herman, M. W., Herrmann, R. B., Benz, H. M., & Furlong, K. P., 2014. Using regional moment tensors to constrain the kinematics and stress evolution of the 2010–2013 Canterbury earthquake sequence, South Island, New Zealand, *Tectonophys.*, **633**, 1–15.

Howell, A., Jackson, J., England, P., Higham, T., & Synolakis, C., 2015. Late Holocene uplift of Rhodes, Greece: evidence for a large tsunamigenic earthquake and the implications for the tectonics of the eastern Hellenic Trench System, *Geophys. J. Int.*, **203**(1), 459–474.

Howell, A., Jackson, J., Copley, A., McKenzie, D., & Nissen, E., 2017. Subduction and vertical coastal motions in the eastern Mediterranean, *Geophys. J. Int.*, **211**, 593–620.

Irmak, T. S., 2013. Focal mechanisms of small-moderate earthquakes in Denizli Graben (SW Turkey), *Earth Planets Space*, **65**(9), 943–955.

Jiménez-Munt, I. & Sabadini, R., 2002. The block-like behavior of Anatolia envisaged in the modeled and geodetic strain rates, *Geophys. Res. Lett.*, **29**(20).

Jónsson, S., Zebker, H., Segall, P., & Amelung, F., 2002. Fault Slip Distribution of the 1999 M_w 7.1 Hector Mine, California, Earthquake, Estimated from Satellite Radar and GPS Measurements, *Bull. Seismol. Soc. Am.*, **92**, 1377–1389.

Jordan, T. H. & Sverdrup, K. A., 1981. Teleseismic location techniques and their application to earthquake clusters in the South-Central Pacific, *Bull. Seismol. Soc. Am.*, **71**, 1105–1130.

Kalafat, D., Gürbüz, C., & Üçer, S. B., 1987. Batı Türkiyede kabuk ve üst manto yapısının araştırılması (in Turkish), *Deprem Araştırma Bülteni*, **59**, 43–64.

Kandilli Observatory and Earthquake Research Institute, Boğaziçi University, 1971. Boğaziçi University Kandilli Observatory and Earthquake Research Institute.

Karasözen, E., Nissen, E., Bergman, E. A., Johnson, K. L., & Walters, R. J., 2016. Normal faulting in the Simav graben of western Turkey reassessed with calibrated earthquake relocations, *J. Geophys. Res.*, **121**, 4553–4574.

Karasözen, E., Nissen, E., Büyükakpınar, P., Cambaz, M. D., Kahraman, M., Ertan, E. K., Abgarmi, B., Bergman, E., Ghods, A., & Özacar, A. A., 2018. The 2017 July 20 M_w 6.6 Bodrum–Kos earthquake illuminates active faulting in the Gulf of Gökova, SW Turkey, *Geophys. J. Int.*, **214**(1), 185–199.

Karasözen, E., Nissen, E., Bergman, E. A., & Ghods, A., 2019. Seismotectonics of the Zagros (Iran) From Orogen-Wide, Calibrated Earthquake Relocations, *J. Geophys. Res.*, **124**(8), 9109–9129.

Kaymakcı, N., Langereis, C., Özkaptan, M., Özacar, A. A., Gülyüz, E., Uzel, B., & Sözbilir, H., 2018. Paleomagnetic evidence for upper plate response to a STEP fault, SW Anatolia, *Earth Planet. Sci. Lett.*, **498**, 101–115.

Kennett, B. L. N., Engdahl, E. R., & Buland, R., 1995. Constraints on seismic velocities in the Earth from traveltimes, *Geophys. J. Int.*, **122**, 108–124.

Kikuchi, M. & Kanamori, H., 1991. Inversion of complex body waves—iii, *Bull. Seismol. Soc. Am.*, **81**(6), 2335–2350.

Kiratzi, A. & Louvari, E., 2003. Focal mechanisms of shallow earthquakes in the Aegean Sea and the surrounding lands determined by waveform modelling: a new database, *J. Geodynamics*, **36**, 251–274.

Koçyiğit, A. & Özacar, A. A., 2003. Extensional neotectonic regime through the NE edge of the outer Isparta Angle, SW Turkey: new field and seismic data, *Turk. J. Earth Sci.*, **12**(1), 67–90.

Kürçer, A., Özdemir, E., Uygun Güldoğan, Ç., & Duman, T. Y., 2016. The First Paleoseismic Trench Data From Acipayam Fault, Fethiye Burdur Fault Zone, SW Turkey, *Bull. Geol. Soc. Greece*, **50**(1), 75–84.

Maggi, A., Priestley, K., & Jackson, J., 2002. Focal Depths of Moderate and Large Size Earthquakes in Iran, *J. Seismol. Earthquake Eng.*, **4**(2–3), 1–10.

Mai, P. M. & Thingbaijam, K. K. S., 2014. SRCMOD: An online database of finite-fault rupture models, *Seismol. Res. Lett.*, **85**(6), 1348–1357.

McCaffrey, R. & Abers, G., 1988. SYN3: A Program for Inversion of Teleseismic Body Wave Forms on Microcomputers, Air force geophysical laboratory technical report, Hanscomb Air Force Base, Massachusetts.

McCaffrey, R., Zwick, P., & Abers, G., 1991. SYN4 Program, Tech. rep., IASPEI Software Library.

McKenzie, D., 1972. Active Tectonics of the Mediterranean Region, *Geophys. J. Int.*, **30**, 109–185.

McKenzie, D., 1978. Active tectonics of the Alpine-Himalayan belt: the Aegean Sea and surrounding regions, *Geophys. J. Int.*, **55**(1), 217–254.

Molnar, P. & Lyon-Caen, H., 1989. Fault plane solutions of earthquakes and active tectonics of the Tibetan Plateau and its margins, *Geophys. J. Int.*, **99**, 123–154.

Mutlu, A. K., 2020. Seismicity, focal mechanism, and stress tensor analysis of the Simav region, western Turkey, *Open Geosciences*, **12**, 479–490.

National Observatory Of Athens, Institute Of Geodynamics, 1997. National Observatory of Athens Seismic Network.

Nissen, E., Ghods, A., Karasözen, E., Elliott, J. R., Barnhart, W. D., Bergman, E. A., Hayes, G. P., Jamal-Reyhani, M., Nemati, M., Tan, F., Abdulnaby, W., Benz, H. M., Shahvar, M. P., Talebian, M., & Chen, L., 2019. The 12 November 2017 M_w 7.3 Ezgeleh-Sarpolzahab (Iran) Earthquake and Active Tectonics of the Lurestan Arc, *J. Geophys. Res.*, **124**(2), 2124–2152.

Nocquet, J.-M., 2012. Present-day kinematics of the Mediterranean: A comprehensive overview of GPS results, *Tectonophys.*, **579**, 220–242.

Ocakoğlu, N., 2012. Investigation of Fethiye-Marmaris Bay (SW Anatolia): seismic and morphologic evidences from the missing link between the Pliny Trench and the Fethiye-Burdur Fault Zone, *Geo-Marine Lett.*, **32**(1), 17–28.

Okada, Y., 1985. Surface deformation due to shear and tensile faults in a half-space, *Bull. Seismol. Soc. Am.*, **75**, 1135–1154.

Över, S., Pınar, A., Özden, S., Yılmaz, H., Ünlügenç, U. C., & Kamacı, Z., 2010. Late cenozoic stress field in the Cameli Basin, SW Turkey, *Tectonophys.*, **492**(1), 60–72.

Över, S., Özden, S., Yilmaz, H., Pinar, A., Ünlügenç, U. C., & Kamaci, Z., 2013a. Plio-Quaternary stress regime in Eşen Çay Basin, SW Turkey, *Geol. Soc. London Spec. Publ.*, **372**, 547–560.

Över, S., Yılmaz, H., Pınar, A., Özden, S., Ünlügenç, U. C., & Kamacı, Z., 2013b. Plio-Quaternary Stress State in the Burdur Basin, SW-Turkey, *Tectonophys.*, **588**, 56–68.

Över, S., Özden, S., Kamacı, Z., Yılmaz, H., Ünlügenç, U. C., & Pınar, A., 2016. Upper crust response to geodynamic processes beneath Isparta Angle, SW Turkey: Revealed by CMT solutions of earthquakes, *Tectonophys.*, **687**, 94–104.

Özbakır, A. D., Şengör, A. M. C., Wortel, M. J. R., & Govers, R., 2013. The Pliny–Strabo trench region: A large shear zone resulting from slab tearing, *Earth Planet. Sci. Lett.*, **375**, 188–195.

Özeren, M. S. & Holt, W. E., 2010. The dynamics of the eastern Mediterranean and eastern Turkey, *Geophys. J. Int.*, **183**(3), 1165–1184.

Özkaptan, M., Kaymakci, N., Langereis, C. G., Gülyüz, E., Özacar, A. A., Uzel, B., & Sözbilir, H., 2018. Age and kinematics of the Burdur Basin: Inferences for the existence of the Fethiye Burdur Fault Zone in SW Anatolia (Turkey), *Tectonophys.*, **744**, 256–274.

Perrin, C., Waldhauser, F., & Scholz, C. H., 2021. The Shear Deformation Zone and the Smoothing of Faults With Displacement, *J. Geophys. Res.*, **126**(5).

Pousse-Beltran, L., Nissen, E., Bergman, E. A., Cambaz, M. D., Gaudreau, É., Karasözen, E., & Tan, F., 2020. The 2020 M_w 6.8 Elazığ (Turkey) Earthquake Reveals Rupture Behavior of the East Anatolian Fault, *Geophys. Res. Lett.*, **47**(13), e88136.

Powers, P. M. & Jordan, T. H., 2010. Distribution of seismicity across strike-slip faults in California, *J. Geophys. Res.*, **115**(B5).

Press, W. H., Teukolsky, S. A., Vetterling, W. T., & Flannery, B. P., 1992. *Numerical Recipes in C: The Art of Scientific Computing*, Cambridge University Press, Cambridge.

Price, S. P. & Scott, B., 1994. Fault-block rotations at the edge of a zone of continental extension; southwest Turkey, *J. Struct. Geol.*, **16**, 381–392.

Reilinger, R., McClusky, S., Vernant, P., Lawrence, S., Ergintav, S., Cakmak, R., Ozener, H., Kadirov, F., Guliev, I., Stepanyan, R., Nadariya, M., Hahubia, G., Mahmoud, S., Sakr, K., ArRajehi, A., Paradissis, D., Al-Aydrus, A., Prilepin, M., Guseva, T., Evren, E., Dmitrotsa, A., Filikov, S. V., Gomez, F., Al-Ghazzi, R., & Karam, G., 2006. GPS constraints on continental deformation in the Africa-Arabia-Eurasia continental collision zone and implications for the dynamics of plate interactions, *J. Geophys. Res.*, **111**.

Reilinger, R. E., McClusky, S. C., Oral, M. B., King, R. W., Toksoz, M. N., Barka, A. A., Kinik, I., Lenk, O., & Sanli, I., 1997. Global Positioning System measurements of present-day crustal movements in the Arabia-Africa-Eurasia plate collision zone, *J. Geophys. Res.*, **102**(B5), 9983–10000.

Ritz, J.-F., Baize, S., Ferry, M., Larroque, C., Audin, L., Delouis, B., & Mathot, E., 2020. Surface rupture and shallow fault reactivation during the 2019 Mw 4.9 Le Teil earthquake, France, *Commun. Earth Environ.*, **1**(1).

Roustaei, M., Nissen, E., Abbassi, M., Gholamzadeh, A., Ghorashi, M., Tatar, M., Yamini-Fard, F., Bergman, E., Jackson, J., & Parsons, B., 2010. The 25 March 2006 Fin earthquakes (Iran) – insights into the vertical extents of faulting in the Zagros Simply Folded Belt, *Geophys. J. Int.*, **181**, 1275–1291.

Savidge, E., Nissen, E., Nemati, M., Karasözen, E., Hollingsworth, J., Talebian, M., Bergman, E., Ghods, A., Ghorashi, M., Kosari, E., Rashidi, A., & Rashidi, A., 2019. The December 2017 Hojedk (Iran) earthquake triplet—sequential rupture of shallow reverse faults in a strike-slip restraining bend, *Geophys. J. Int.*, **217**(2), 909–925.

Shaw, B. & Jackson, J., 2010. Earthquake mechanisms and active tectonics of the Hellenic subduction zone, *Geophys. J. Int.*, **181**, 966–984.

Sokos, E. & Zahradník, J., 2013. Evaluating Centroid-Moment-Tensor Uncertainty in the New Version of ISOLA Software, *Seismol. Res. Lett.*, **84**(4), 656–665.

Sokos, E. N. & Zahradník, J., 2008. ISOLA a Fortran code and a Matlab GUI to perform multiple-point source inversion of seismic data, *Computers & Geosciences*, **34**, 967–977.

Taymaz, T. & Price, S., 1992. The 1971 May 12 Burdur earthquake sequence, SW Turkey: a synthesis of seismological and geological observations, *Geophys. J. Int.*, **108**, 589–603.

Taymaz, T., Jackson, J., & Westaway, R., 1990. Earthquake mechanisms in the Hellenic Trench near Crete, *Geophys. J. Int.*, **102**, 695–731.

Taymaz, T., Jackson, J., & McKenzie, D., 1991. Active tectonics of the north and central Aegean Sea, *Geophys. J. Int.*, **106**, 433–490.

Taymaz, T., Wright, T. J., Yolsal, S., Tan, O., Fielding, E., & Seyitoğlu, G., 2007. Source characteristics of the 6 June 2000 Orta Cankiri (central Turkey) earthquake: a synthesis of seismological, geological and geodetic (InSAR) observations, and internal deformation of the Anatolian plate, *Geol. Soc. London Spec. Publ.*, **291**(1), 259–290.

Technological Educational Institute Of Crete, 2006. Seismological Network of Crete.

ten Veen, J. H., 2004. Extension of Hellenic forearc shear zones in SW Turkey: the Pliocene-Quaternary deformation of the Eșen Çay Basin, *J. Geodynamics*, **37**(2), 181–204.

Tiryakioğlu, I., Floyd, M., Erdoğan, S., Gülal, E., Ergintav, S., McClusky, S., & Reilinger, R., 2013. GPS constraints on active deformation in the Isparta Angle region of SW Turkey, *Geophys. J. Int.*, **195**(3), 1455–1463.

Tosun, L., Avşar, U., Avşar, Ö., Dondurur, D., & Kaymakcı, N., 2021. Active tectonics and kinematics of Fethiye-Göcek Bay, SW Turkey: Insight about the eastern edge of Pliny-Strabo Trenches, *J. Struct. Geol.*, **145**.

Tur, H., Yaltırak, C., Elitez, I., & Sarıkavak, K. T., 2015. Pliocene-Quaternary tectonic evolution of the Gulf of Gökova, southwest Turkey, *Tectonophys.*, **638**, 158–176.

Walker, R. T., Bergman, E. A., Szeliga, W., & Fielding, E. J., 2011. Insights into the 1968-1997 Dasht-e-Bayaz and Zirkuh earthquake sequences, eastern Iran, from calibrated relocations, InSAR and high-resolution satellite imagery, *Geophys. J. Int.*, **187**, 1577–1603.

Wells, D. L. & Coppersmith, K. J., 1994. New Empirical Relationships among Magnitude, Rupture Length, Rupture Width, Rupture Area, and Surface Displacement, *Bull. Seismol. Soc. Am.*, **84**(4), 974–1002.

Wessel, P., Smith, W. H. F., Scharroo, R., Luis, J., & Wobbe, F., 2013. Generic Mapping Tools: Improved Version Released, *Eos Trans. AGU*, **94**, 409–410.

Weston, J., Engdahl, E. R., Harris, J., Di Giacomo, D., & Storchak, D. A., 2018. ISC-EHB: reconstruction of a robust earthquake data set, *Geophys. J. Int.*, **214**(1), 474–484.

Wimpenny, S. & Watson, C. S., 2021. gWFM: A Global Catalog of Moderate-Magnitude Earthquakes Studied Using Teleseismic Body Waves, *Seismol. Res. Lett.*, **92**(1), 212–226.

Woodside, J., Mascle, J., Huguen, C., & Volkonskaia, A., 2000. The Rhodes Basin, a post-Miocene tectonic trough, *Marine. Geol.*, **165**, 1–12.

Wright, T. J., Parsons, B. E., Jackson, J. A., Haynes, M., Fielding, E. J., England, P. C., & Clarke, P. J., 1999. Source parameters of the 1 October 1995 Dinar (Turkey) earthquake from SAR interferometry and seismic bodywave modelling, *Earth Planet. Sci. Lett.*, **172**, 23–37.

Wright, T. J., Lu, Z., & Wicks, C., 2003. Source model for the M_w 6.7, 23 October 2002, Nenana Mountain Earthquake (Alaska) from InSAR, *Geophys. Res. Lett.*, **30**(18).

Wright, T. J., Gonzalez, P. J., Walters, R. J., Hatton, E. L., Spaans, K., & Hooper, A. J., 2016. LiCSAR: Tools for automated generation of Sentinel-1 frame interferograms, *AGU Fall Meeting Abstr.*.

Yang, J., Xu, C., Wang, S., & Wang, X., 2020. Sentinel-1 observation of 2019 M_w 5.7 Acipayam earthquake: A blind normal-faulting event in the Acipayam basin, southwestern Turkey, *J. Geodynamics*, **135**.

Yılmaztürk, A. & Burton, P. W., 1999. Earthquake source parameters as inferred from the body waveform modeling, southern Turkey, *J. Geodynamics*, **27**(4), 469–499.

Yolsal-Çevikbilen, S., Taymaz, T., & Helvacı, C., 2014. Earthquake mechanisms in the Gulfs of Gökova, Sığacık, Kuşadası, and the Simav Region (western Turkey): Neotectonics, seismotectonics and geodynamic implications, *Tectonophys.*, **635**, 100–124.

Zahradník, J. & Sokos, E., 2018. ISOLA Code for Multiple-Point Source ModelingReview, in *Moment Tensor Solutions*, ed. Damico, S., Springer, Cham.

Zahradnik, J., Jansky, J., & Plicka, V., 2008. Detailed Waveform Inversion for Moment Tensors of $M \sim 4$ Events: Examples from the Corinth Gulf, Greece, *Bull. Seismol. Soc. Am.*, **98**(6), 2756–2771.

Zwick, P., McCaffrey, R., & Abers, G., 1994. MT5 Program, *IASPEI Software Library*, **4**.

Table 1. Source parameters of the 2017 Arıcılar foreshock and mainshock and the 2019 Acıpayam and Bozkurt mainshocks from catalogues (GCMT = Global Centroid Moment Tensor project; USGS = United States Geological Survey ANSS Comprehensive Earthquake Catalog (ComCat); RMT = Regional Moment Tensor solution), other published studies, and from our own modelling. The listed origin times are those yielded by calibrated earthquake relocations. Location refers to the latitude and longitude of the GCMT and GEOFON centroids, the USGS epicenter, the relocated epicenter for our seismological solutions, and the peak slip patch our InSAR solutions (surface projection coordinates of our InSAR model fault planes are listed separately in Supplementary Table S1). Depth refers to the centroid depth for all of the seismological solutions, and the depth of peak slip for our InSAR solutions.

Event	Source	Location	Strike	Dip	Rake	Depth	Moment (Nm)	M_w
Arıcılar	GCMT	37.04°, 28.47°	130°	57°	−65°	12 km	5.48×10^{16}	5.1
2017-11-22	USGS W-phase	37.051°, 28.643°	82°	32°	−130°	11.5 km	5.04×10^{16}	5.1
20:22:52	GEOFON	37.05°, 28.64°	120°	38°	−75°	10 km	–	5.0
	This study (regional waveforms)	37.1125°, 28.5984°	91°	34°	−128°	2 km	4.00×10^{16}	5.0
Arıcılar	GCMT	37.03°, 28.60°	105°	49°	−82°	12 km	9.73×10^{16}	5.3
2017-11-24	USGS W-phase	37.085°, 28.622°	106°	43°	−85°	11.5 km	8.24×10^{16}	5.2
21:49:15	USGS RMT	37.085°, 28.622°	110°	46°	−80°	3 km	5.61×10^{16}	5.1
	GEOFON	37.00°, 28.57°	112°	41°	−76°	10 km	–	5.3
	This study (InSAR)	37.1212°, 28.6127°	92°	45°	−88°	1.8 km	1.47×10^{17}	5.4
	This study (regional waveforms)	37.1009°, 28.6146°	87°	21°	−140°	1 km	9.99×10^{16}	5.3
Acıpayam	GCMT	37.37°, 29.38°	321°	42°	−87°	12 km	4.04×10^{17}	5.7
2019-03-20	USGS W-phase	37.408°, 29.531°	326°	50°	−87°	17.5 km	4.57×10^{17}	5.7
06:34:27	USGS body wave	37.408°, 29.531°	320°	50°	−88°	6 km	2.48×10^{17}	5.5
	USGS RMT	37.408°, 29.531°	314°	47°	−80°	12 km	4.62×10^{17}	5.7
	GEOFON	37.46°, 29.48°	310°	45°	−99°	16 km	–	5.7
	Yang et al. (2020) (InSAR)	37.43°, 29.38°	332°	44°	−76°	6 km	–	5.7
	Elliott et al. (2020) (InSAR)	37.444°, 29.426°	336°	58°	−70°	6.1 km	3.12×10^{17}	5.6
	This study (InSAR)	37.4595°, 29.4152°	326°	54°	−80°	6.1 km	3.09×10^{17}	5.6
	This study (teleseismic body waveforms)	37.4331°, 29.4570°	328°	44°	−88°	6 km	2.44×10^{17}	5.5
	This study (regional waveforms)	37.4331°, 29.4570°	324°	43°	−76°	7 km	3.49×10^{17}	5.6
Bozkurt	GCMT	37.81°, 29.68°	275°	35°	−94°	14.7 km	8.27×10^{17}	5.9
2019-08-08	USGS W-phase	37.935°, 29.700°	289°	38°	−80°	15.5 km	7.59×10^{17}	5.9
11:25:29	USGS body wave	37.935°, 29.700°	286°	36°	−80°	9 km	5.81×10^{17}	5.8
	USGS RMT	37.935°, 29.700°	277°	34°	−82°	10 km	5.45×10^{17}	5.8
	GEOFON	37.91°, 29.75°	279°	33°	−95°	16 km	–	5.9
	This study (InSAR)	37.8750°, 29.6962°	270°	32°	−96°	8.5 km	9.14×10^{17}	5.9
	This study (teleseismic body waveforms)	37.8821°, 29.6408°	254°	35°	−95°	12 km	4.46×10^{17}	5.7
	This study (regional waveforms)	37.8821°, 29.6408°	283°	38°	−84°	10 km	6.43×10^{17}	5.8

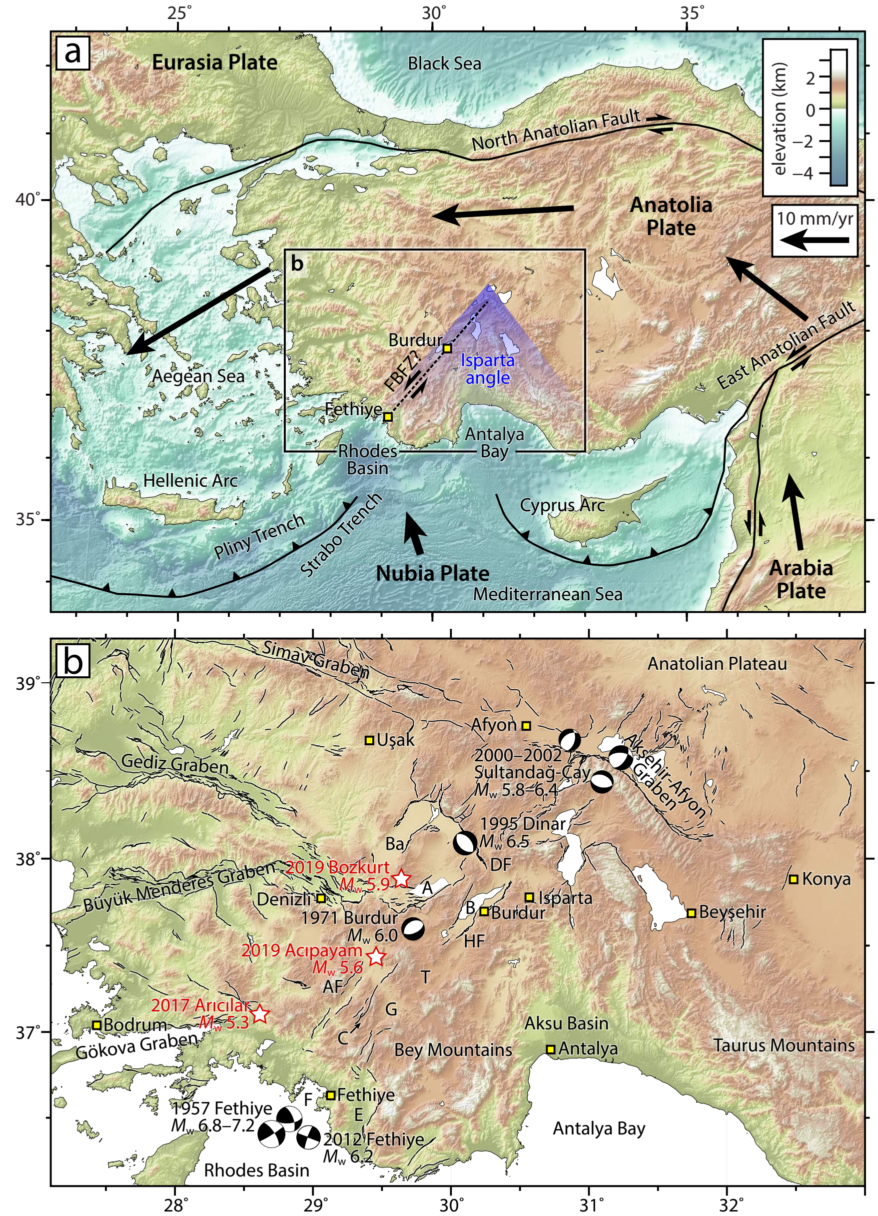

Figure 1. (a) Regional tectonic setting. Black lines denote major plate boundary faults, and thick black arrows show representative motions of the Anatolia, Nubia and Arabia plates with respect to Eurasia (Reilinger et al. 2006). The Isparta angle is shaded in blue and the generalized trend of the purported Fethiye-Burdur Fault Zone (FBFZ) is marked by a dashed line. (b) Major tectonic structures and mapped active faults across southwestern Turkey, from the national active fault database of Emre et al. (2018). Tectonic features discussed in Section 2 are labelled as follows: the Gulf of Fethiye (F), Eşen-Çay basin (E), Çameli basin (C), Gölhisar basin (G), Teffeni basin (T), Burdur basin (B), Acıgöl basin (A), Baklan basin (Ba), Acıpayam fault (AF), Hacılar fault (HF) and the Dinar fault (DF). Red stars show epicenters of the 2017 Arıcılar and 2019 Acıpayam and Bozkurt earthquakes, and black focal mechanisms are for the earlier instrumental earthquakes discussed in Section 2. Yellow squares show major cities along the Fethiye-Burdur trend.

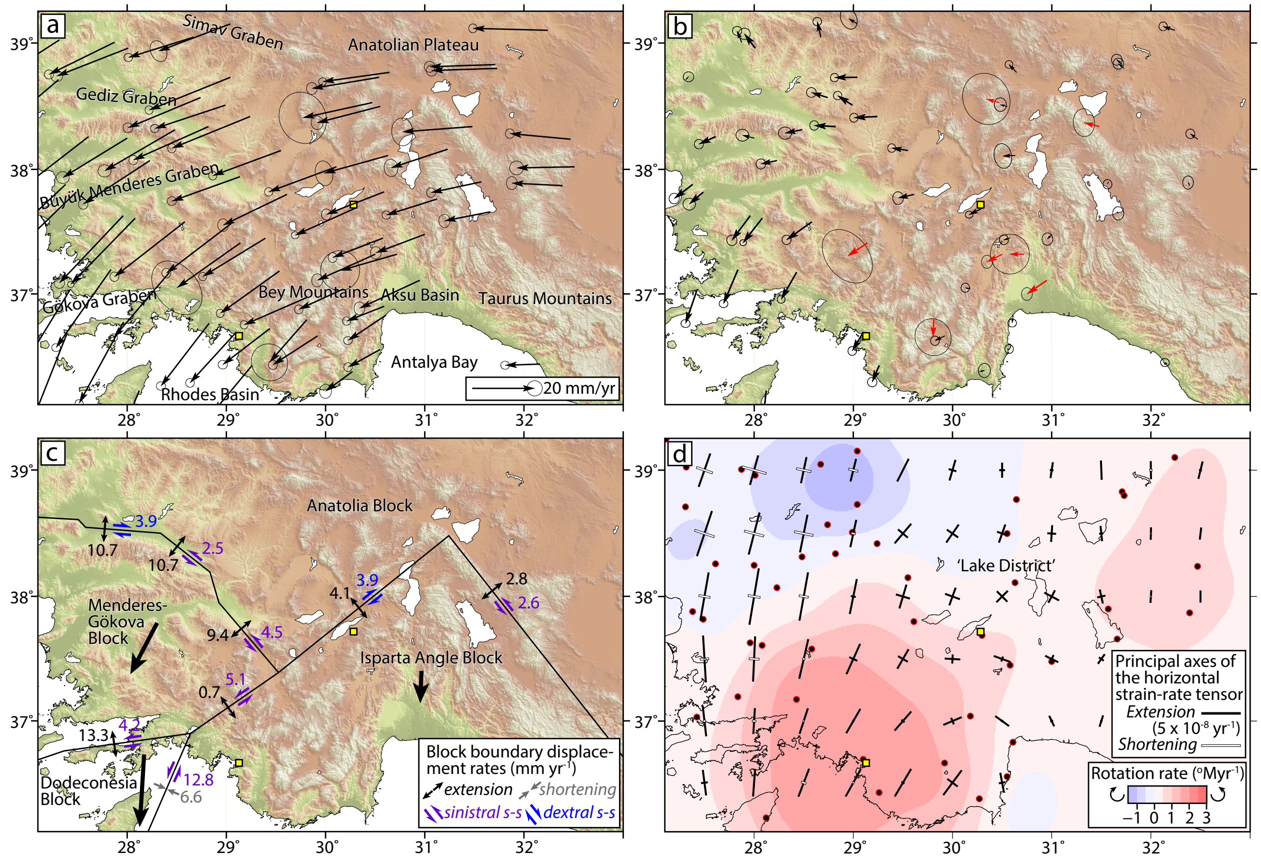

Figure 2. GNSS velocities and derived tectonic models for southwestern Turkey (figure adapted from Howell et al. (2017)). Yellow squares are the cities of Fethiye and Burdur and the topography is as in Figure 1. (a) GNSS velocities and 2σ uncertainties, showing data from Nocquet (2012) and Tiryakioğlu et al. (2013) placed into the same fixed Eurasia reference frame (see Howell et al. (2017) for details). (b) GNSS velocities with respect to stable Anatolia. Red vectors show stations with large uncertainties or suspected non-tectonic displacement that were excluded from Howell et al.'s (2017) analysis. (c) GNSS-derived block model boundaries and slip-rates (in mm yr^{-1}) from Tiryakioğlu et al. (2013). Thick black arrows show generalized block motions with respect to Anatolia. (d) GNSS-derived strain rate field from Howell et al. (2017). Colours indicate vertical axis rotation rates; bars indicate principal axes of the horizontal strain rate tensor, with extension in black and contraction in white; and black circles show GNSS datapoints used in the analysis.

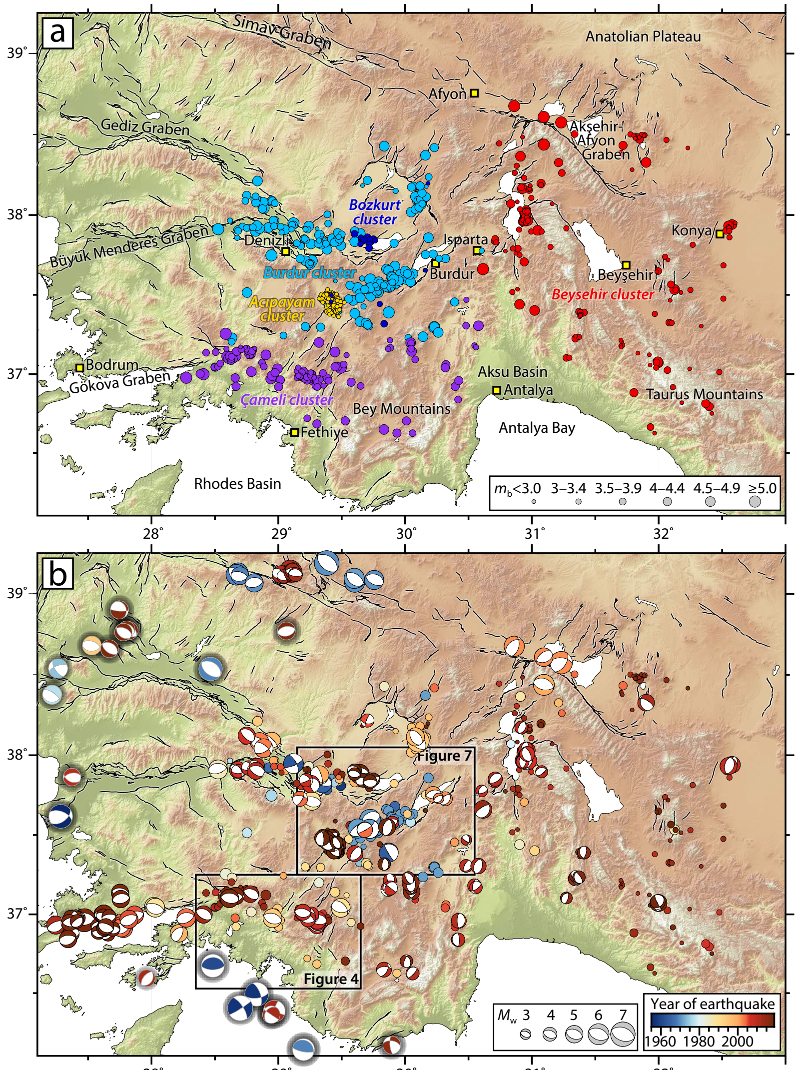

Figure 3. (a) Earthquake epicenters relocated in this study, scaled by magnitude and coloured by cluster. Magnitudes are those listed by the International Seismological Centre, mostly m_b. Active faults are from the national database of Emre et al. (2018) and topography is as in Figure 1. (b) Relocated earthquake focal mechanisms (beach balls) and epicenters (circles) coloured by year of occurrence and scaled by magnitude (epicenters as in (a), and focal mechanisms scaled separately by M_w). We only plot earthquakes whose best available focal or centroid depths are ≤35 km, which excludes a few deeper events, in particular in Antalya Bay. Note that the thrust and strike-slip earthquakes in the Rhodes basin, including four early instrumental events with poorly-constrained depths, are interpreted to have ruptured subducting Nubian rather than overriding Anatolian lithosphere (McKenzie 1972; Howell et al. 2017). Relocated earthquakes in the Simav and Gökova graben are from Karasözen et al. (2016, 2018); earthquakes lacking relocated epicenters (in the Gediz and Büyük Menderes graben and the Rhodes basin) are marked with shadows.

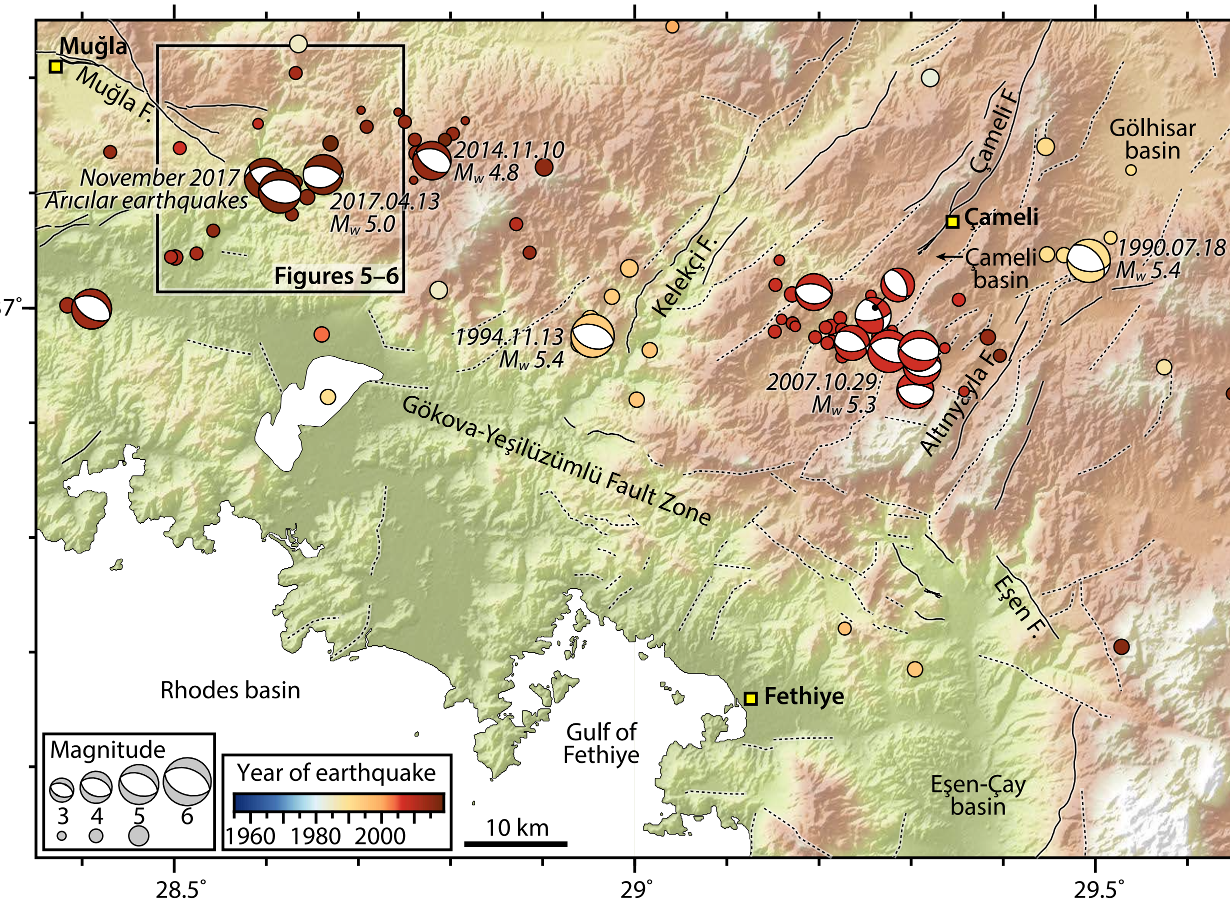

Figure 4. Relocated earthquake focal mechanisms and epicenters in the region north of Fethiye (at the southwestern end of the Fethiye-Burdur trend), coloured by year of occurrence and scaled by magnitude as in Figure 3b. Topography is as in Figure 1. Solid lines show the national active fault database of Emre et al. (2018); dashed lines are additional faults from Alçiçek et al. (2006), Alçiçek (2007), Elitez & Yaltırak (2014), and Elitez et al. (2017).

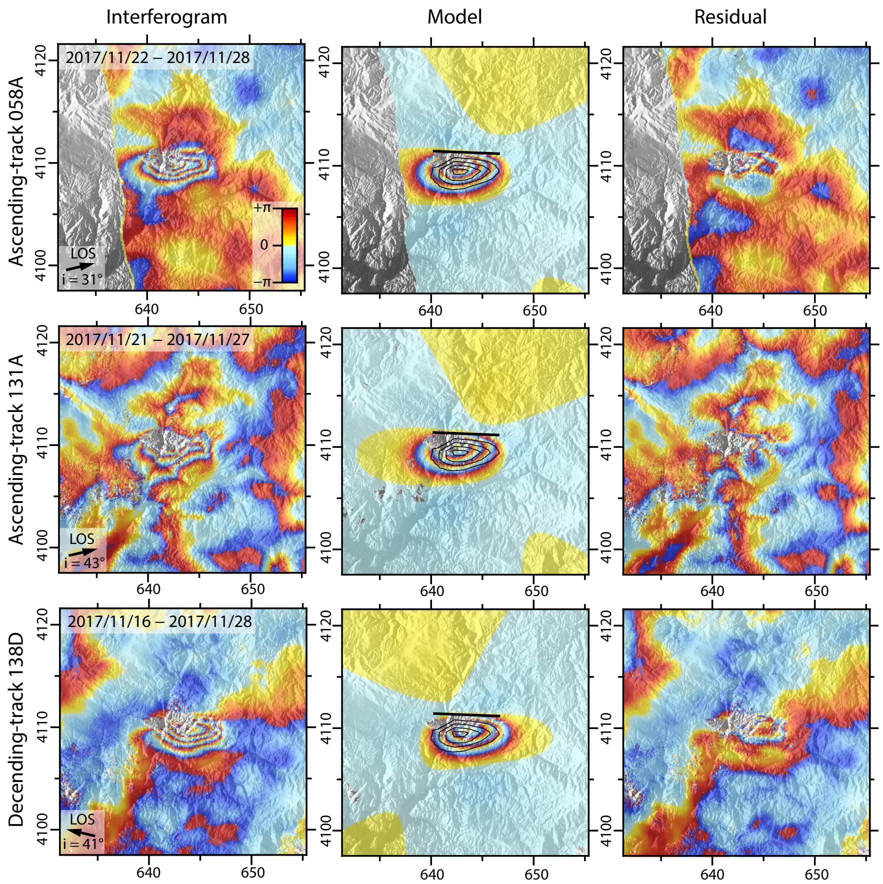

Figure 5. (a) Data (left column), model (center) and residual (right) interferograms for the 22–24 November 2017 M_w 5.1 and 5.3 Arıcılar earthquakes on ascending track 58A (upper row), ascending track 131A (middle row), and descending track 138D (lower row). Coordinates are UTM Zone 35 kilometers and the InSAR imagery is plotted over artificially-shaded topography. LOS is the satellite line-of-sight, i is the off-nadir incidence angle in the region of interest, and 2π radians in phase change is equivalent to 2.77 cm of deformation relative to the satellite. In the model panels, the contours show 8 cm slip increments on the buried model fault plane and the thick black line shows its surface projection.

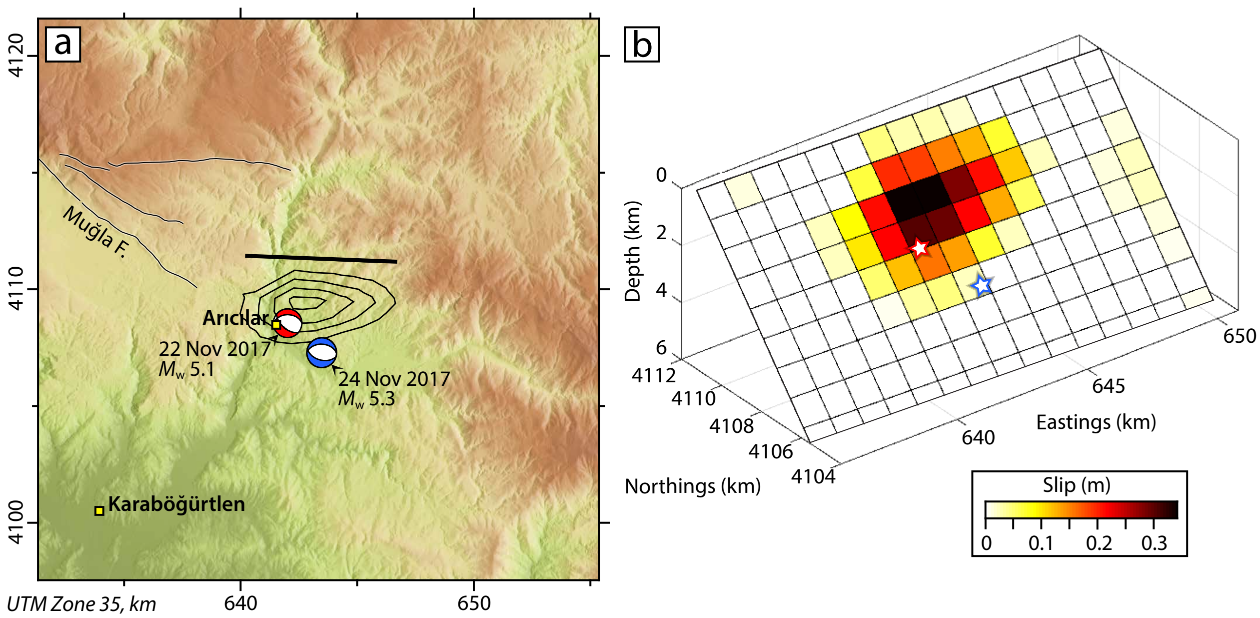

Figure 6. Relocated focal mechanisms of the 22 November 2017 Arıcılar M_w 5.1 foreshock (red) and the 24 November 2017 M_w 5.3 mainshock (blue). Contours show 8 cm slip increments on the buried model fault plane and the thick black line shows its surface projection. Other active faults are from Emre et al. (2018) and topography is as in Figure 1. (b) InSAR model slip distribution of the Arıcılar earthquake (tabulated in Supplementary Table S2). Relocated epicenters of the 22 November foreshock (red star) and 24 November mainshock (blue star) are shown projected vertically onto the InSAR model fault plane.

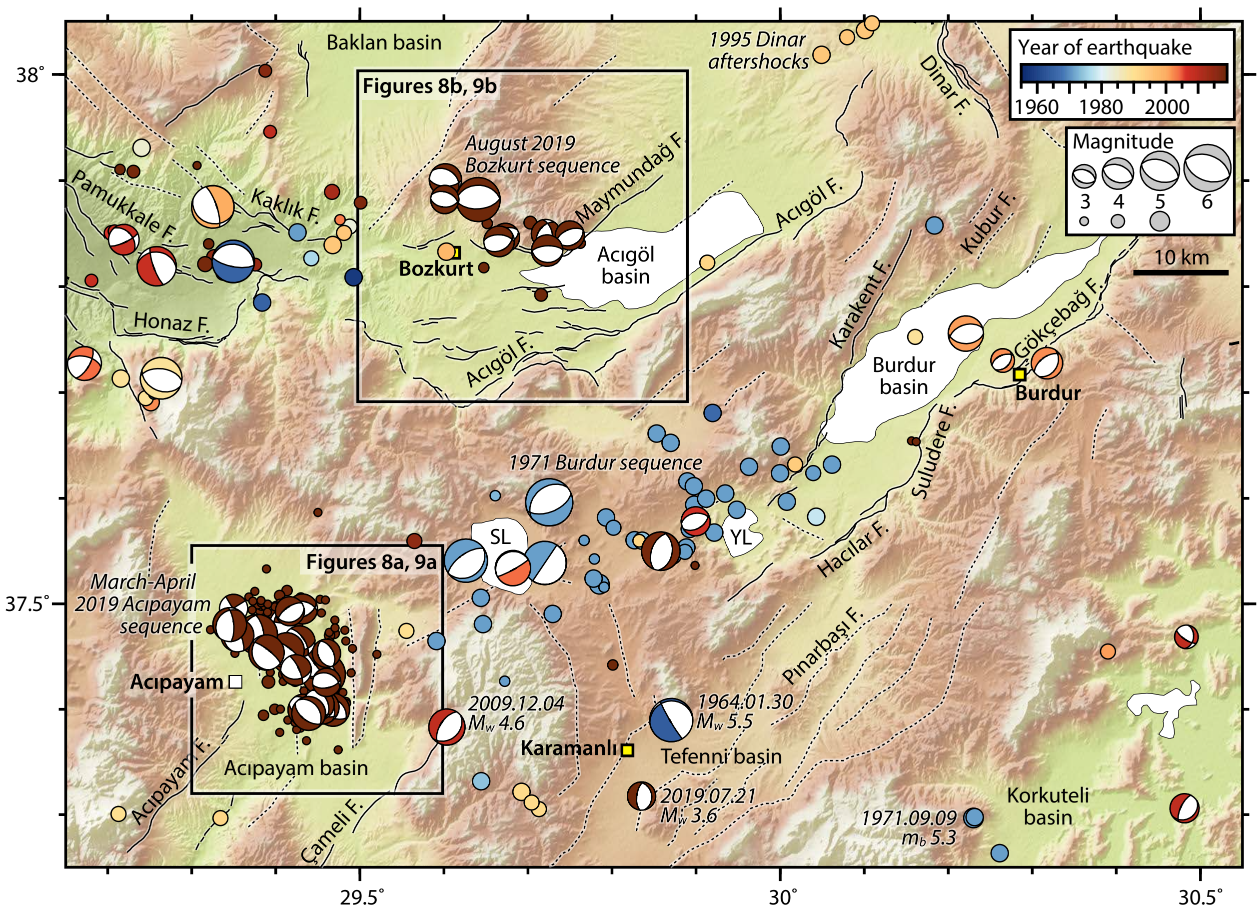

Figure 7. Relocated earthquake focal mechanisms and epicenters in the region west of Burdur (along the northeastern Fethiye-Burdur trend), coloured by year of occurrence and scaled by magnitude as in Figure 3b. Topography is as in Figure 1. Solid lines show the national active fault database of Emre et al. (2018); dashed lines mark a few additional faults from Taymaz & Price (1992), Alçiçek et al. (2006), Alçiçek et al. (2013), Aksoy & Aksarı (2016) and Elitez & Yaltırak (2016). For the 12 May 1971 M_w 6.0 Burdur mainshock, only the first sub-event is shown; the second has a similar mechanism but its relative location is unconstrained (Taymaz & Price 1992). SL = Salda Lake and YL = Yarışlı Lake.

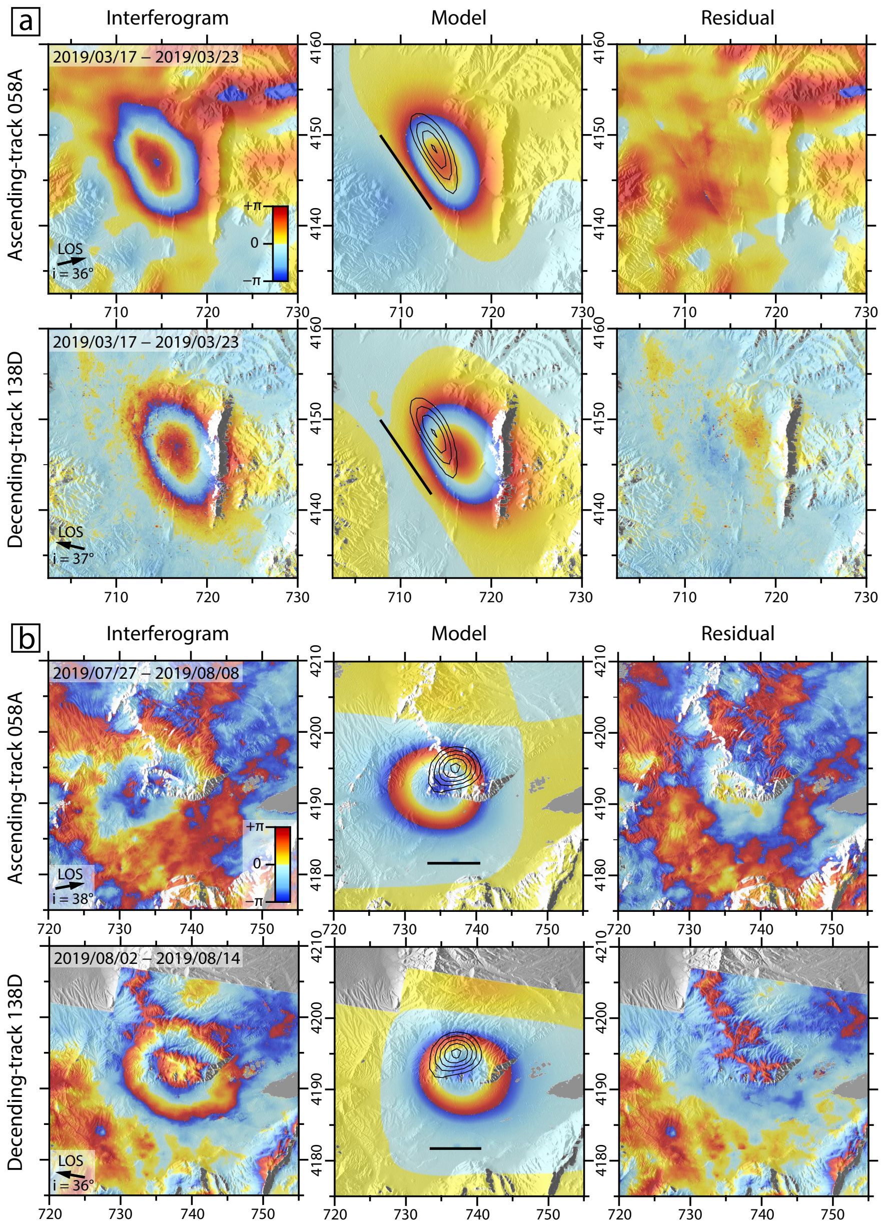

Figure 8. (a) Data (left column), model (center) and residual (right) interferograms for the 20 March 2019 M_w 5.6 Acıpayam earthquake on ascending track 58A (upper row) and descending track 138D (lower row). Coordinates are UTM Zone 35 kilometers and the InSAR imagery is plotted over artificially-shaded topography. LOS is the satellite line-of-sight, i is the off-nadir incidence angle in the region of interest, and 2π radians in phase change is equivalent to 2.77 cm of deformation relative to the satellite. In the model panels, the contours show 8 cm slip increments on the buried model fault plane and the thick black line shows its surface projection. (b) Data, model and residual interferograms for the 8 August 2019 M_w 5.9 Bozkurt earthquake. The layout is the same as in (a), except that the slip contours in the model interferograms are at 12 cm increments.

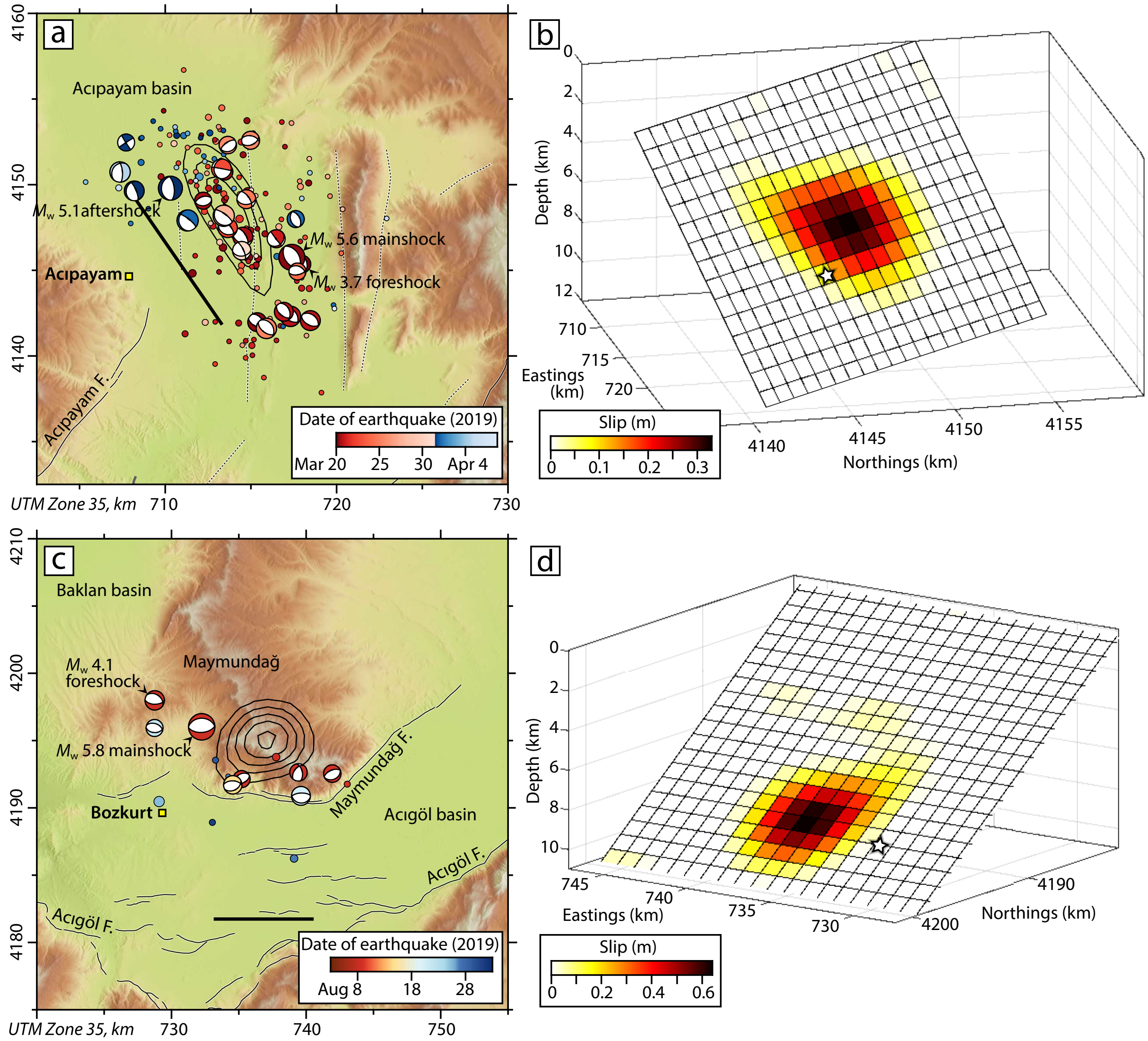

Figure 9. (a) Relocated earthquake focal mechanisms and epicenters of the March–April 2019 Acıpayam sequence. Events are coloured by date, with those occurring before the largest (M_w 5.1) aftershock in shades of red and those after it in shades of blue. Contours show 8 cm slip increments on the buried, InSAR model fault plane and the thick black line shows its surface projection. Thinner solid lines are active faults from Emre et al. (2018) and dashed lines are additional faults from Alçiçek et al. (2006) and Elitez & Yaltırak (2016). (b) InSAR model slip distribution of the 20 March 2019 M_w 5.6 Acıpayam mainshock (tabulated in Supplementary Table S3). (c) Relocated earthquake focal mechanisms and epicenters of the August 2019 Bozkurt sequence, coloured by date. The layout is the same as in (a), except that contours show 12 cm model slip increments. (d) InSAR model slip distribution of the 8 August 2019 M_w 5.9 Bozkurt mainshock (tabulated in Supplementary Table S5).

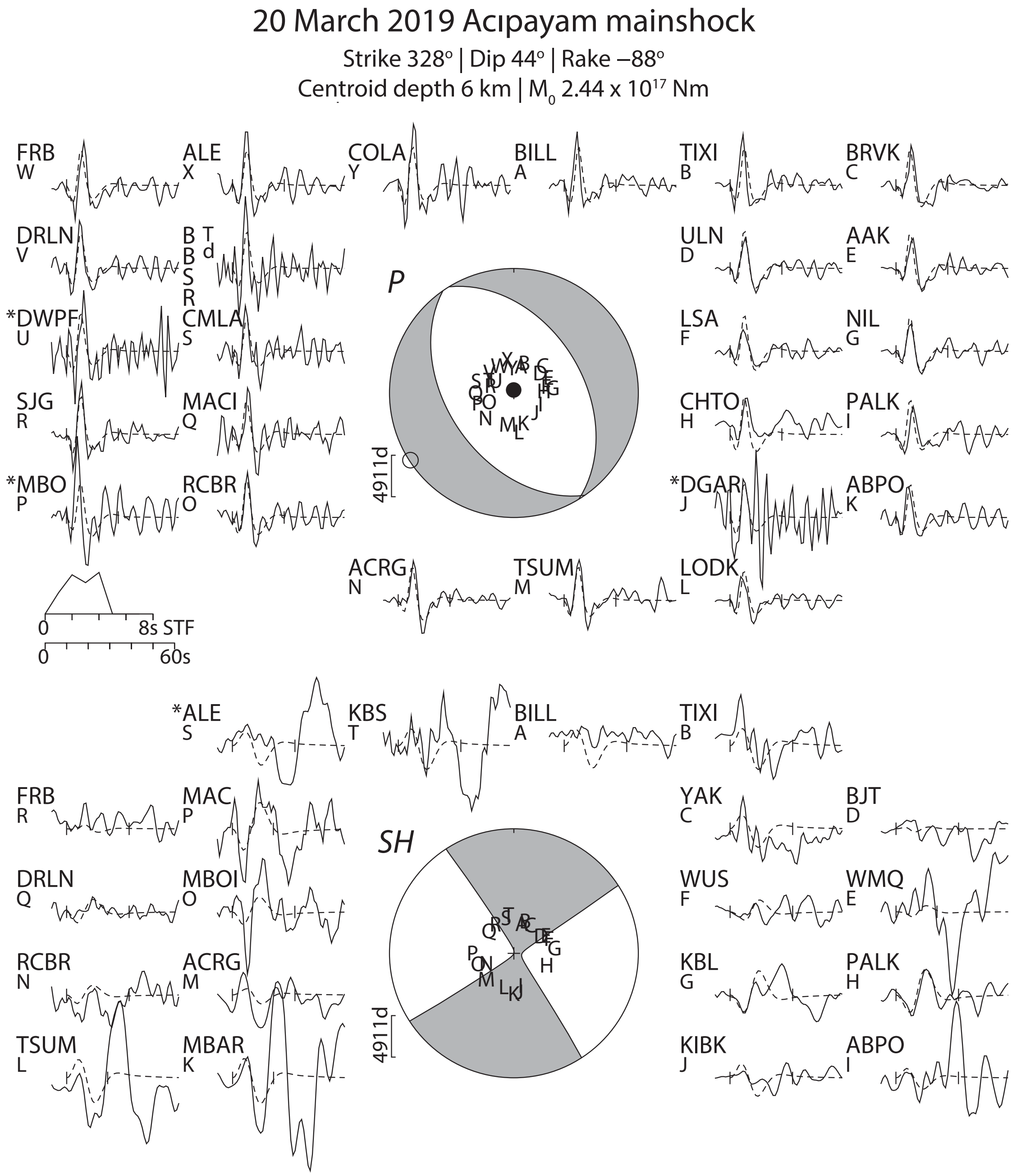

Figure 10. Long period teleseismic body waveform model of the 20 March 2019 Acıpayam mainshock. The upper part of each panel shows the *P* focal sphere and vertical component seismograms, the lower part shows the *SH* focal sphere and transverse component seismograms, and the source-time function and a waveform time scalebar are shown on the left. On each focal sphere, we plot nodal planes (lines), station positions (capital letters), and P and T axes (solid and open circles). Outside the focal sphere, we plot observed (solid) and synthetic (dashed) seismograms, with station codes and focal sphere station position letters to the left of each. Stations with asterisks are considered too noisy to be included in the inversion, but are shown for reference. Vertical ticks mark the *P* or *SH* arrival time and the inversion window end.

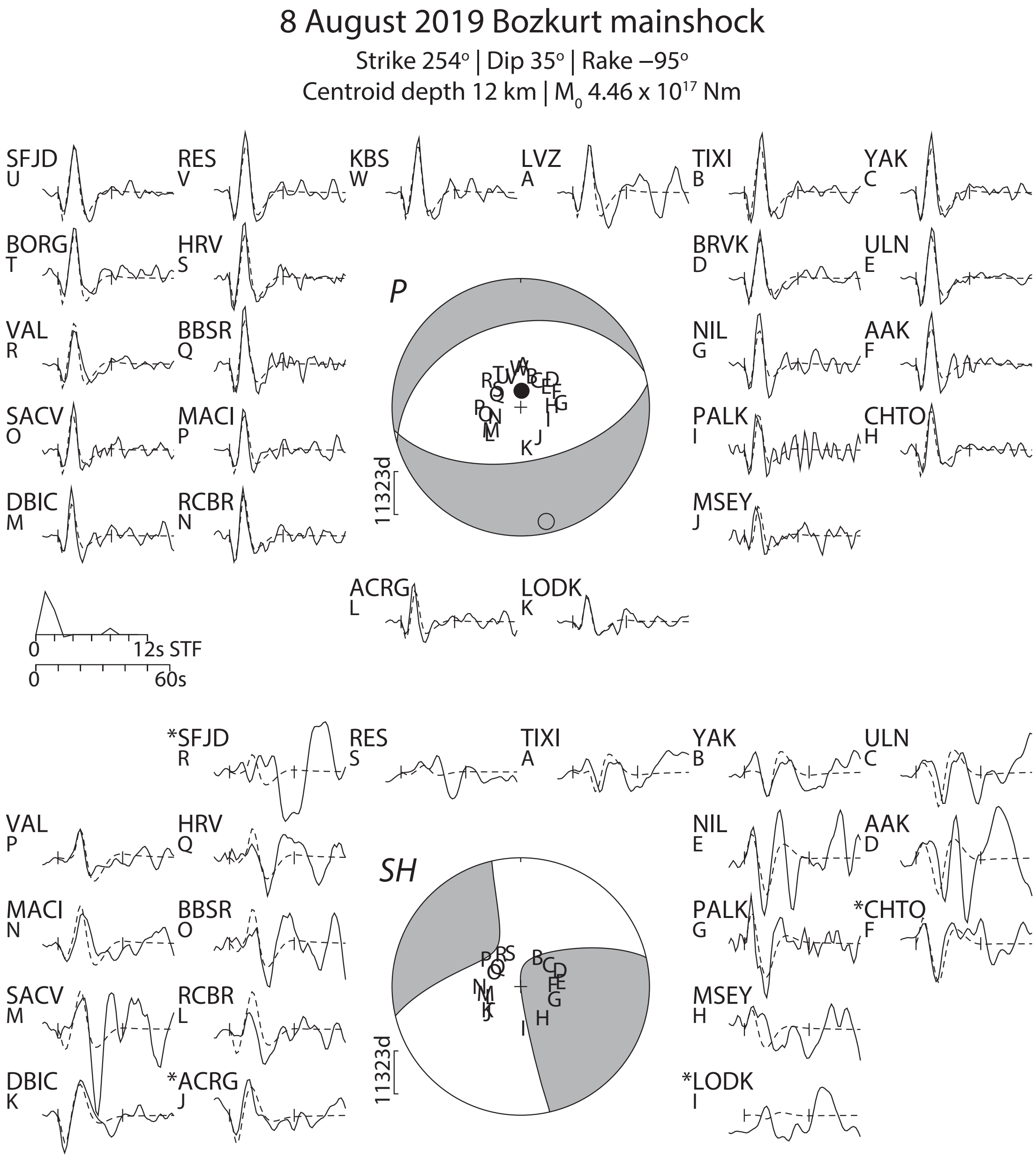

Figure 11. Long period teleseismic body waveform model of the 8 August 2019 Bozkurt mainshock. The layout is as in Figure 10.